DESIGN OF HELICOPTER TRANSMISSION OIL COOLING FAN IMPELLER WITH MULTI-OBJECTIVE OPTIMIZATION METHOD

A THESIS SUBMITTED TO
THE GRADUATE SCHOOL OF NATURAL AND APPLIED SCIENCES
OF
MIDDLE EAST TECHNICAL UNIVERSITY

BY

GÖKHAN AVŞAR

IN PARTIAL FULFILLMENT OF THE REQUIREMENTS
FOR
THE DEGREE OF MASTER OF SCIENCE
IN
AEROSPACE ENGINEERING

JANUARY 2023

Approval of the thesis:

DESIGN OF HELICOPTER TRANSMISSION OIL COOLING FAN IMPELLER WITH MULTI-OBJECTIVE OPTIMIZATION METHOD

submitted by **GÖKHAN AVŞAR** in partial fulfillment of the requirements for the degree of **Master of Science** i**n Aerospace Engineering, Middle East Technical University** by,

Prof. Dr. Halil Kalıpçılar
Dean, Graduate School of **Natural and Applied Sciences** _____

Prof. Dr. Serkan Özgen
Head of the Department, **Aerospace Engineering** _____

Assist. Prof. Dr. Özge Başkan Perçin
Supervisor, **Aerospace Engineering, METU** _____

Examining Committee Members:

Prof. Dr. Oğuz Uzol
Aerospace Engineering, METU _____

Assist. Prof. Dr. Özge Başkan Perçin
Aerospace Engineering, METU _____

Prof. Dr. Kahraman Albayrak
Mechanical Engineering, METU _____

Prof. Dr. Sinan Eyi
Aerospace Engineering. METU _____

Assist. Prof. Dr. Onur Baş
Mechanical Engineering, TEDU _____

Date: 18.01.2023

I hereby declare that all information in this document has been obtained and presented in accordance with academic rules and ethical conduct. I also declare that, as required by these rules and conduct, I have fully cited and referenced all material and results that are not original to this work.

Name Last name : Gökhan Avşar

Signature :

ABSTRACT

DESIGN OF HELICOPTER TRANSMISSION OIL COOLING FAN IMPELLER WITH MULTI-OBJECTIVE OPTIMIZATION METHOD

Avşar, Gökhan
Master of Science, Aerospace Engineering
Supervisor: Assist. Prof. Dr. Özge Başkan Perçin

January 2023, 74 pages

This study aims to optimize the impeller geometry of a backward-curved blade centrifugal fan in a helicopter oil cooler to improve the aerodynamic performance of the impeller. The study consists of three main parts: aerodynamic design and parametrization of the impeller, numerical analysis of impeller performance, and multi-objective design optimization to maximize fan static pressure and total to static isentropic efficiency. In the first part, a one-dimensional impeller design is performed using quasi-experimental methods and a direct optimization method with the multi-objective genetic algorithm, and the impeller geometry is parameterized through a commercial tool. The three-dimensional flow through the impeller is solved in the second part with a commercial computational fluid dynamics tool. The Reynolds-Averaged Navier-Stokes equations are solved on a multi-block grid, and a second-order accurate finite volume method is employed. The most appropriate turbulence model and grid size are selected considering time, cost, and fidelity. In the third part, a sensitivity analysis is performed with the design-of-experiment method, and the parameters that affect the objective function most significantly are determined. A multi-objective design optimization based on a non-dominated sorting

genetic algorithm is performed with the Kriging Response Surface Method, and pareto optimal solutions are obtained. Results show that, at the design point, there is a 9.6% and 0.96% increase in the fan static pressure and total to static isentropic efficiency, respectively. The trained Kriging response surface model predicts the fan static pressure and total to static isentropic efficiency with an error of 0.12% and 0.33%, respectively.

Keywords: Helicopter, Oil Cooling Fan, Centrifugal fan, Optimization, Genetic Algorithm,

ÖZ

HELİKOPTER TRANSMİSYON YAĞ SOĞUTMA FAN ÇARKININ ÇOK AMAÇLI OPTİMİZASYON YÖNTEMİ İLE TASARIMI

Avşar, Gökhan
Yüksek Lisans, Havacılık ve Uzay Mühendisliği
Tez Yöneticisi: Dr. Öğr. Üyesi Özge Başkan Perçin

Ocak 2023, 74 sayfa

Bu çalışma, helikopter trasmisyon yağının soğutulması için kullanılan geriye eğik kanatlı bir salyangoz fan çarkı tasarımının optimizasyonunu amaçlamaktadır. Çalışma 3 ana bölümden oluşmaktadır: çark tasarımı ve parametrizasyonu, sayısal analizler ile performans hesabı ve fan statik basıncı ve izantropik verimliliği en üst düzeye çıkarmak için çok amaçlı tasarım optimizasyonu. Birinci bölümde, yarı deneysel yöntemler ve Çok Amaçlı Genetik Algoritma ile Direkt Optimizasyon yöntemi kullanılarak tek boyutlu çark tasarımı yapılmış ve çark geometrisi ticari bir yazılım aracılığıyla parametreleştirilmiştir. İkinci bölümde, çarktan geçen üç boyutlu akış ticari bir hesaplamalı akışkanlar dinamiği aracılığıyla çözülmüştür. Reynolds-Averaged Navier-Stokes denklemleri çok bloklu ağ kullanılarak ve ikinci derece çözünürlükte sonlu hacimler prensibiyle çözülmüştür. Zaman, maliyet ve uygunluk dikkate alınarak en uygun türbülans modeli ve grid boyutu seçilir. Üçüncü bölümde, deney tasarımı yöntemi ile duyarlılık analizi yapılarak amaç fonksiyonu en çok etkileyen parametreler belirlenir. Kriging Tepki Yüzey Yöntemi ile Baskın Olmayan Sıralama Genetik Algoritmasına dayalı çok amaçlı bir tasarım optimizasyonu gerçekleştirilmiş ve Pareto-optimal çözümler elde edilmitşir. Sonuçlar, tasarım

noktasında fan statik basıncında ve toplam-statik izantropik verimde sırasıyla %9.6 ve %0.96'lık bir artış olduğunu göstermektedir. Eğitilen Kriging Tepki Yüzey Yöntemi modeli, sırasıyla %0.12 ve %0.33'lük bir hatayla fan statik basıncını ve toplam-statik izantropic verimliliği tahmin eder.

Anahtar Kelimeler: Helikopter, Yağ Soğutma Fanı, Salyangoz Fan, Optimizasyon, Genetik Algoritma

Dedication

To my lovely family Şebnem, Simba and Joey

ACKNOWLEDGMENTS

The author would like to thank his supervisor Assist. Prof. O. Başkan PERÇİN for her guidance, advice, criticism, encouragement, and insight throughout the research.

The author would like to thank Ahmet Alper EZERTAŞ for his suggestions and technical comments. He would also like to thank his chief engineer, Halil İbrahim ÜNLÜ, for allowing him to work flexible hours and for his patience.

The author would also like to thank everyone who worked for UNMER HAVALANDIRMA, which contributed a lot to his education and profession.

TABLE OF CONTENTS

LIST OF TABLES

TABLES

LIST OF FIGURES

FIGURES

LIST OF ABBREVIATIONS

ABBREVIATIONS

ANN	Artificial Neural Network
BC	Backward Curved
BPNN	Back Propagation Neural Network
CCD	Central Composite Design
CFD	Computational Fluid Dynamics
DF	Diffusion Factor
DH	De Haller
DoE	Design of Experiment
GA	Genetic Algorithm
FC	Forward Curved
LSCC	Low-Speed Centrifugal Compressor
MOEA	Multi-Objective Evolutionary Algorithm
NSGA	Non Sorting Genetic Algorithm
OD	Orthogonal Design
POF	Pareto Optimal Front
RANS	Reynolds Averaged Navier Stokes
RBNN	Radial Basis Neural Network
RSM	Response Surface Methodology
SA	Spalart Allmaras
SST	Shear Stress Transport

LIST OF SYMBOLS

SYMBOLS

c	Absolute Velocity [m/s]
D	Outlet Diameter [m]
Q	Volumetric Flow Rate [m^3/s]
u	Tangential Velocity [m/s]
w	Relative Velocity
η	Isentropic efficiency
σ	Speed number
δ	Diameter number
ΔP	Fan Static Pressure [Pa]
ρ	Density [kg/m^3]
β	Blade Angle [°]

CHAPTER 1

INTRODUCTION

Centrifugal fans are used in many areas such as heating, cooling, ventilation and dust collection units and helicopter oil cooling in todays. Since helicopter operation is critical, helicopter systems such as transmission gearbox, engine and electrical generator, are frequently lubricated and cooled using separate oil supplies. However, separated oil supplies may be cooled with a fan. Air/Oil coolers are effectively used in many helicopters such as Chinook – 47, AW189 [1], AW139, UH-60, and AS332.

The centrifugal fan, which can be seen in Figure 1, consists of two essential parts: an impeller and a volute. Flow enters the centrifugal fan parallel to the rotation axis. When air flows through the blade passages, it is directed toward the tip of the impeller. This causes a 90° rotation in the flow direction in the meridional plane and an increase in the pressure. Pressurized air leaving the impeller enters the spiral structure, the volute, where it travels at a constant speed to the exit. Based on the direction of the blade curvature, centrifugal fans can be categorized as having either forward curved (FC), backward curved (BC), or radial blades, as indicated in Figure 2. Aside from their compact size and low noise, the highest pressure rise and highest flow rate are two specific advantages of forward curved fans among the centrifugal fans with the same rotational speed and diameter. Their power increases as the flow rate increases. Because of high blade loading, the number of blades are between 30-60. On the other hand, fans with backward-curved or radial blades typically have 6-16 blades, a narrower width, and a longer chord length. Although forward-curved and radial centrifugal impellers provide high absolute velocity, backward-curved centrifugal fans have a high static efficiency. Because head loss is proportional to

absolute velocity squared, BC centrifugal fans are the most efficient [2]. It is crucial to design the BC centrifugal fan to maximize efficiency.

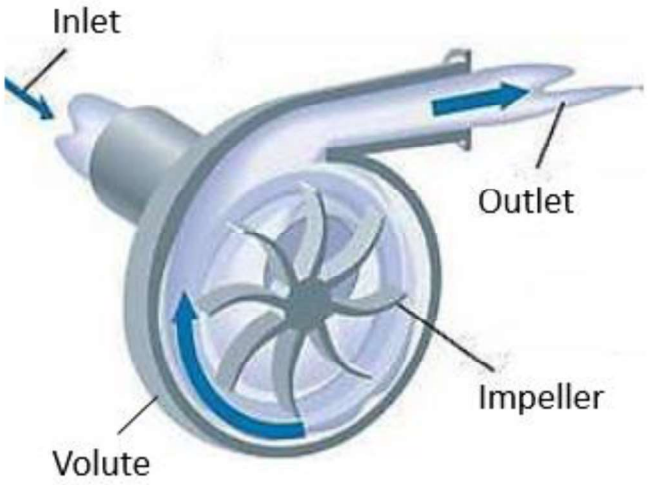

Figure 1. Centrifugal fans are composed of two main parts: an impeller and a volute. The blue arrows show the direction of the flow in the fan. (Reproduced from [3])

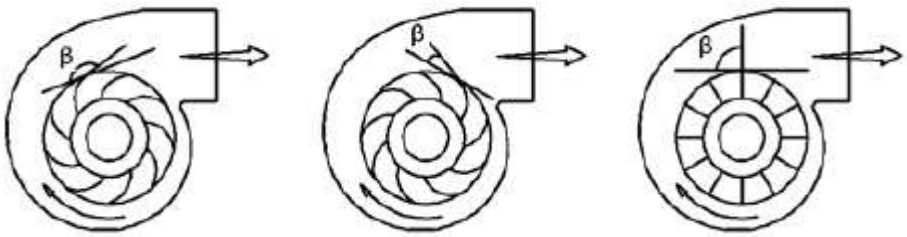

Figure 2. Centrifugal fan with forward-curved (FC) (left), backward-curved (BC) (middle) radial blades (right) [4]

1.1 Aim of the Thesis

The energy efficiency of turbomachines, which are frequently used in areas where high electricity is consumed (industry, etc.), is an important parameter that should guide the design. A study conducted in the USA in 2002 showed that turbomachines constitute 22-27% of industrial electricity consumption [5]. In the oil cooling fans of

helicopters, a rise in efficiency reduces fuel consumption and the drag caused by fan intake and while increasing payload. It's also crucial to note that the temperature of an electrical generator has a direct effect on the efficiency of the generator's performance. Therefore, provided mass flow rate and fan efficiency are crucial for air-cooled electric generators. For these reasons, it is crucial to design high-efficiency fans to increase energy savings and minimize the effects on nature.

The purpose of this research is to determine the design parameters of a centrifugal fan impeller used to cool helicopter oil and optimize its performance by increasing fan static pressure and total to static isentropic efficiency. Fan static pressure ΔP_{ts} and total-to-static efficiency η_{ts} are given in Equations 1.1 and 1.2, respectively:

$$\Delta P_{ts} = P_{s2} - P_{t1} \tag{1.1}$$

$$\eta_{ts} = \frac{\left(\frac{P_{s2}}{P_{t1}}\right)^{(\gamma-1)/\gamma} - 1}{\left(\frac{T_{t2}}{T_{t1}}\right) - 1} \tag{1.2}$$

where P_s is the static pressure, P_t the total pressure, T_t the total temperature and γ the ratio of specific heats. Subscripts 1 and 2 stand for the inlet and outlet of the impeller, respectively.

Considering that the entropy generation in the impeller is higher than that in the volute [6], the study concentrates on the aerodynamic optimization of the impeller.

1.2 Literature Review

There are many studies in the literature on centrifugal fan design. In some studies [7], [8], experiments are conducted to assess the fan performance, and fan design parameters that affect the performance most are determined based on the performance of several fans with different geometries. Since that approach causes a lot of time, effort, and cost, today, numerical methods are preferred instead of experimental ones [9]. Design optimization coupled with Computational Fluid

Dynamics (CFD), a widely used method in turbomachinery design, comes to the fore among numerical analysis methods due to its efficiency in time and cost [10]. Considering the studies in the literature, centrifugal fan optimization mainly focuses on two aspects: improving the meridional profile [11]–[16] and investigating the effect of blade design parameters on fan performance, such as inlet/outlet width and inlet/outlet blade angle [9], [10], [17], [18]. The former is known as shape optimization, and the latter is size optimization. Only one study will be discussed to give insight into impeller shape optimization.

Kim et al. [14], used a hybrid multi-objective evolutionary algorithm (MOEA) with a surrogate model to optimize the design of a centrifugal impeller. While keeping the leading edge and trailing edge of the impeller fixed, four points on the meridional contour defined by the Bezier curve were selected for parametrization, which is shown in Figure 3. In their study, Radial Basis Neural Network was used to evaluate objective functions pressure ratio and isentropic efficiency. Pareto Optimum Fronts (POF) were obtained with the use of NSGA-II, and these POFs contain two endpoints that efficiency was increased by 0.65% and 0.19%, and the PR was increased by 0.86% and 1.40 Evidence from this study shows that the present optimization, which combines a hybrid MOEA and RANS analysis, was a valuable technique for determining the optimal form of a centrifugal impeller blade.

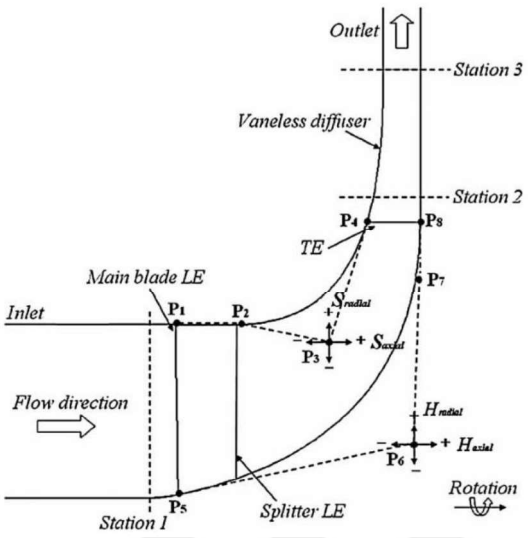

Figure 3. Centrifugal impeller meridional view [14]

Heo et al. [10], conducted a study with the goal of optimizing efficiency and pressure by adjusting the location of the splitter blade and the ratio of their inlet and outlet widths. Using the Response Surface Approximation model and a multi-objective evolutionary algorithm, a Pareto optimal solution (POS) was generated. The surrogate model is trained with thirteen design points using Latin Hypercube Design. Flow domain computations were performed using the ANSYS TurboSystem tools BladeGen, TurboGrid and CFX. k-ω Shear Stress Transport (SST) was used as the turbulence closure model. The research found that the fan blade without the splitter blade increased efficiency by about 6.7% and static pressure by about 8.7%.

In the study conducted by Zhang et al. [17], a model to predict centrifugal fan performance parameters was constructed using multi-objective optimization design relied on orthogonal design (OD) and the Back Propagation Neural Network (BPNN). The number of blades, blade outlet stagger angle and width were selected as the design variables, with efficiency and total pressure increase as the objective functions. The developed model predicts pressure and efficiency with an error of 0.97% and 0.33%, respectively. The results show that predictive values and sample values are almost equal (Figure 4). A genetic algorithm was used to find the optimum centrifugal fan blade design. As can be seen in Figure 5 (a), there was an upward

shift in total pressure, and an increase of 6.91% in total pressure at the design point. The high-efficiency area was broadened and efficiency is increased by 0.5% at the design point, as shown in Figure 5 (b). Moreover, BPNN was discovered to be an efficient surrogate model that can be used to optimize centrifugal fan performance.

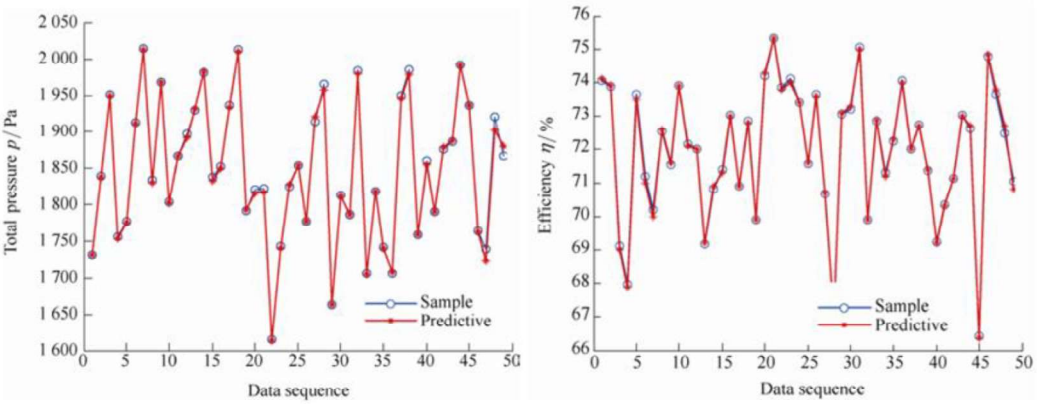

Figure 4. Comparisons of the sample and predicted total pressure (left) and efficiency (right) values inferred from the fan performance prediction model established in Ref. [17]

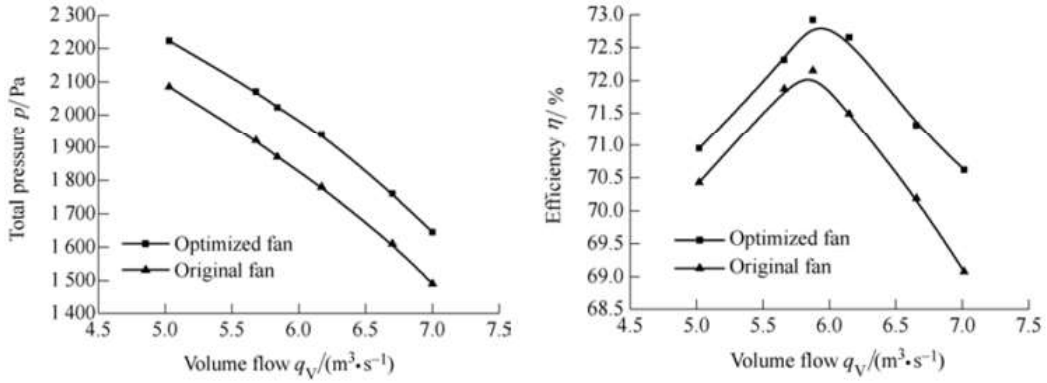

Figure 5. Fan performance curves obtained from numerical simulations performed in Ref. [17]: Total pressure vs. volumetric flow rate (left) and efficiency vs. volumetric flow rate (right)

In the study of Meng et al. [18], an impeller of a backward-curved centrifugal fan was optimized using response surface methodology by maximizing efficiency. The inlet blade angle, the exit blade angle, and the total number of blades are all three design variables. Box-Behnken Design was a Design of Experiment technique used for selecting sample points. Using least squares regression, response surface data

was fitted. As a result, centrifugal fan efficiency was increased by 1.4%, as shown in Table 1.

Table 1. RSM optimization and CFD result

	RSM Optimization Result	CFD Optimization Result	Original Fan
Efficiency η	93.70%	93.60%	92.07%

Unlike other studies, in the study by Zhu and Qin [9], the potential for the use of RSM in turbomachinery was examined. The inlet radius and blade outlet height were chosen as design variables and efficiency and pressure were chosen as objective functions. Firstly, RSM was built with a single design space by fitting all experimental data to a polynomial equation of second-order. Design of Experiment (DoE) was implemented using a full factorial design approach. In other words, the RSM result did not match the test results. As a solution, the design area was divided into four sub-regions, and the efficiency and pressure increase for each area were found separately, as seen in Figure 6. The optimization findings were consistent with the test results. Genetic Algorithm produced the best results for each RSM function after fitting surrogate models, as shown in Table 2. As a result, the RSM was determined to be an effective and appropriate surrogate model. This method was found to significantly reduce objective function complexity and overall optimization time.

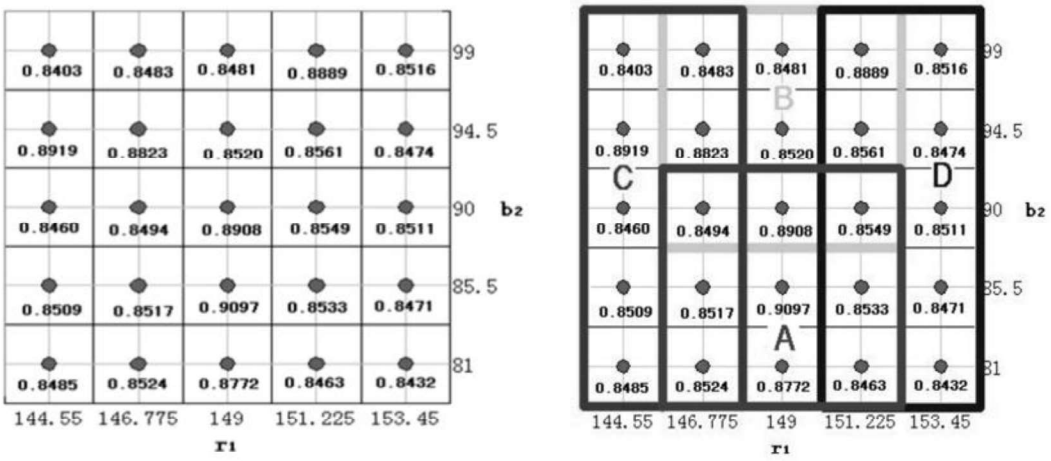

Figure 6. The test points and their responses. Response surface equations for the whole zone (left) and for each sub-zone (right) differ from each other. Therefore, the optimum of each sub-zone is different than the optimum of the whole zone [9]

Table 2. Genetic algorithm calculation results (reproduced from [9]).

Serial Number	r_1 (mm)	b_2 (mm)	η
A	151.2	86.8	0.906
B	148.7	90.8	0.874
C	146.77	91.4	0.864
D	151.26	98.9	0.88

In his MSc thesis at the Department of Aerospace Engineering at METU, Çevik designed and optimized a mixed-flow compressor impeller [19]. The study consists of the following parts, 1D design of the centrifugal impeller, optimization, impeller modelling, and Computational Fluid Dynamics analysis of the optimized impeller. The design period began with defining the engine's performance requirements, followed by calculating the required compressor performance using an engine parametric cycle design code. To optimize the specific thrust and decrease thrust-specific fuel consumption, blade exit angle, blade tip depth, incidence angle, rotor inlet diameter ratio, and rotor meridional exit angle were selected as design variables. The Neural Network algorithm was trained using a dataset generated by DoE orthogonal arrays to approximate functions. Finally, mixed-flow impeller design optimization was performed by a multi-directional search algorithm. In this study, a

turbojet engine which has a typical radial compressor was compared with a turbojet engine with an optimized mixed-flow impeller, and the results are presented in Table 3. The results demonstrate an 11% improvement in thrust and a 13% improvement in thrust-specific fuel consumption.

Table 3. Comparison of the optimized mixed-flow compressor-based turbojet performance with radial compressor-based turbojet performance

Parameters	A turbojet engine with a typical radial compressor	Current Design	Difference [%]
Mass Flow Rate (kg/s)	0.36	0.388	8
Pressure Ratio	3.1	4.34	40
Thrust (N)	216	240	11
TSFC (kg/sec/N)	6.20E-05	5.38E-05	-13
Flight Mach Number	0.3	0.3	-

The preliminary results of the current study were presented in Ref [20]. In this study, pressure ratio and efficiency were taken into account when performing multi-objective optimization on a centrifugal fan impeller. NSGA-II and Kriging-based RSM were employed as the optimization algorithm and surrogate model, respectively. Design-of-experiment study was performed using Latin Hypercube Design. 53 design points were employed to train the response surface. At the design point, the pressure ratio increased by 3.14%, and an increase was observed at all mass flow rates considered. However, although the efficiency was slightly increased (1.16%) at the design point, a decrease in efficiency was observed for higher mass flow rates.

A summary of the literature review is given in Table 4. Centrifugal impeller studies in the literature focus on either shape optimization by improving the meridional profile or size optimization by changing the design parameters including inlet/outlet width, blade angle and blade number. There are two objective functions for centrifugal fan impeller optimization in the literature; maximizing pressure rise and/or efficiency. If multi-objective optimization is desired, both can be selected as objectives using the weight constant or by obtaining a pareto optimal front. As a

surrogate model and optimization algorithm, Response Surface Method and evolution-based algorithms are generally used, respectively.

Table 4. Centrifugal impeller optimization literature summary

Investigators	DoE	Design Variables	Objective Functions	Surrogate Model	Optimization Algorithm	Results/Achievement
Man-Woong Heo, Jin-Hyuk Kim and Kwang-Yong Kim [10]	LHS	-the impeller's inlet and outlet height ratio -the position of splitter blades	Efficiency pressure rise	Response Surface Model	Evolutionary Algorithm	6.6% increase in efficiency 8% increase in pressure
ZHANG Lei, WANG Songling, HU Chenxing, and ZHANG Qian [17]	Orthogonal Design	-Blade number -Exit stagger angle -Impeller outlet width	Total pressure Efficiency	BP neural network	Genetic Algorithm	6.91% increase in total pressure 0.5% increase in efficiency The fan noise is reduced.
Changyun Zhu, Guoliang Qin [9]	Full Factorial Design	-Inlet Radius (r1) -impeller outlet width(b2)	Efficiency	Response Surface Model	Genetic Algorithm	RSM is found an effective method.
J-H Kim, J-H Choi, A Husain, and K-Y Kim [14]	LHS	Bezier Control Points	Isentropic Efficiency Pressure Ratio	Radial Basis Neural Network	NSGA-II	The isentropic efficiency and pressure ratio are improved in design and off-design situations.
Fannian Meng, Quanlin Dong, Yan Wang, Pengfei Wang and Chunxi Zhang [18]	BBD	-inlet and outlet blade angle -blade number	Efficiency	Response Surface Model	-	1.66% increase in efficiency
Mert Çevik, Oğuz Uzol and İbrahim Sinan Akmandor [19]	Orthogonal Array	-Blade Exit Angle -Blade tip depth -Incidence Angle -Rotor Inlet Diameter Ratio -Rotor meridional Exit Angle	Maximizing Specific thrust Minimizing TSFC	Neural Network - Leuvenberg-Marquardt	Direct Search Algorithm	11% increase in Thrust 13% decrease in TSFC
Gökhan Avşar, Alper Ezertaş and Özge Başkan Perçin [20]	LHS	Tip Radius Inlet Height Outlet Height Tip Width Hub Inlet Angle Hub Outlet Angle Shroud Inlet Angle Shroud Outlet Angle	Pressure Ratio Isentropic Efficiency	Response Surface Model	Genetic Algorithm	3.15% increase in PR 1.16% increase in Efficiency

1.3 Methodology

Using ANSYS DesignXplorer, a commercial multi-objective optimization algorithm coupled with CFD simulations, this study optimizes the aerodynamic design of a

backward-curved centrifugal fan impeller. The road map of the study is shown in Figure 7. The methodology consists of preliminary impeller design, CFD analysis, and optimization. Preliminary design is performed in VistaCCD based on several input parameters, including the pressure ratio (PR), mass flow rate, rotational speed, and other geometric constraints. The impeller model is created by transferring the preliminary design to the BladeGen tool, which allows the meridional profile, blade angle, and blade thickness distribution to be adjusted. The geometry that has been created is then transferred to the BladeEditor for parametrization. The inlet and outlet width, axial length, and tip radius are selected as preliminary inputs for the sensitivity analysis study. After the impeller is designed, the computational mesh is generated in the TurboGrid tool for the numerical simulations. High-fidelity CFD analyses are performed using the ANSYS CFX. After numerical calculations are completed, the baseline analysis set is transferred to the ANSYS DesignXplorer optimization tool. First, in the DoE part, sensitivity analysis is performed, and the design parameters that primarily affect the objective function are determined. Then, the meta-model is trained using design points selected by DoE. The study of centrifugal fan design optimization is carried out with the goal of maximizing fan static pressure and total-to-static isentropic efficiency. The Pareto Optimal Solution is discovered as a result of the optimization study, and one candidate is chosen from among them. Fan static pressure, and total to static isentropic efficiency curves are plotted for the optimum solution and compared with the baseline set.

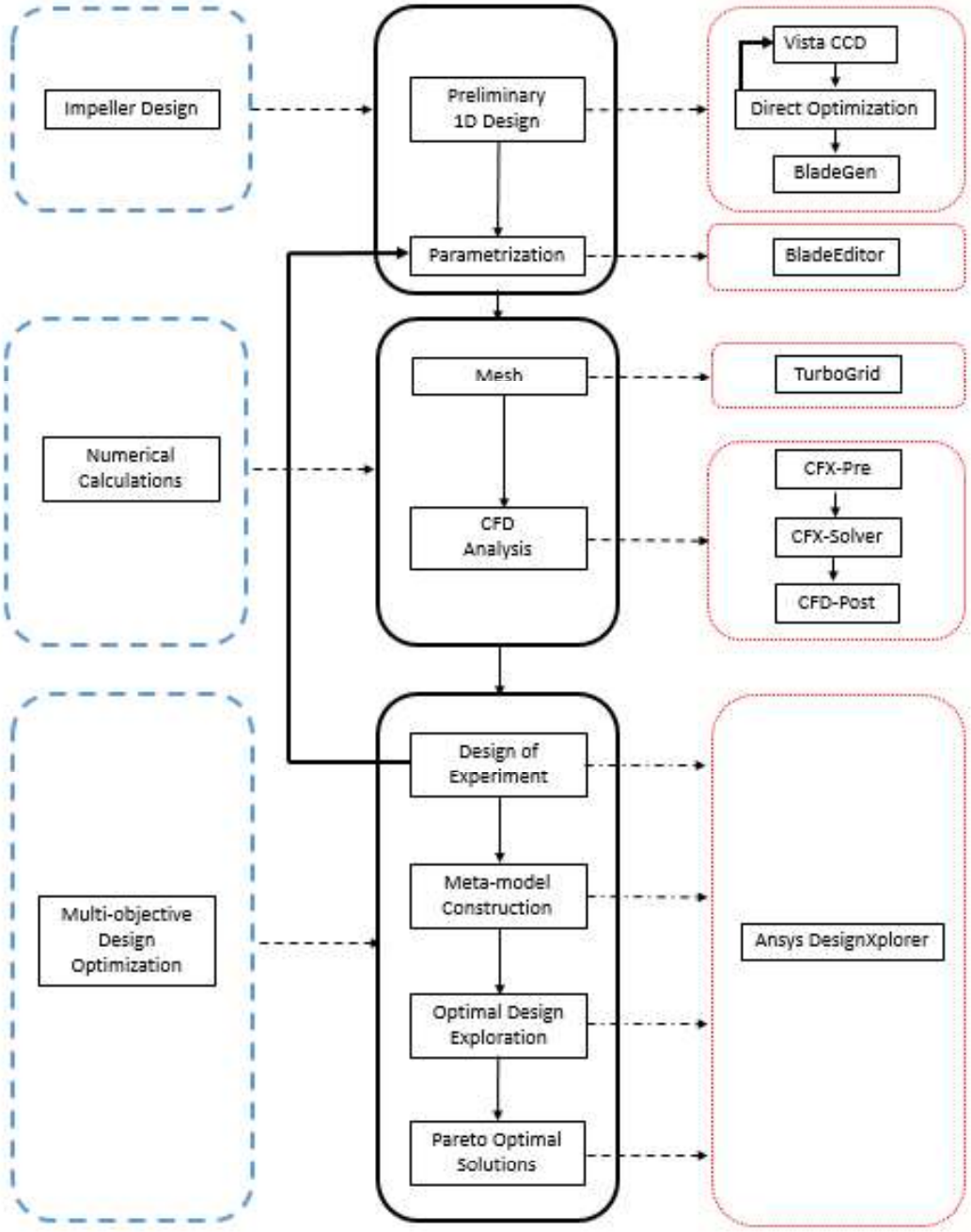

Figure 7. The centrifugal fan impeller design optimization roadmap consists of three main parts: Impeller design, numerical calculations, and multi-objective design optimization.

CHAPTER 2

AERODYNAMIC OPTIMIZATION

Optimization is the procedure of finding the best solution to a problem while satisfying certain constraints. In design optimization, design variables (or design parameters), design space, constraints, and the objective function are the main components of optimization. In a design process, any engineering system is defined by a set of quantities, and these quantities are known as preassigned parameters if they are fixed during the automated design process. It implies that the designer is not free to select specific parameters. Design variables are all other quantities that are treated as variables during the design process. In other words, design variables can be changed. Design variables can be either continuous or discrete. A design value is referred to as continuous if it is free to assume any value within a specified bound, or discrete if it can only assume preset values within a predefined set. Design constraints are the constraints that must be met to produce an acceptable design [21]. As an example, the maximum power required by a centrifugal fan may be limited. The objective function is a set of criteria that the designer hopes to achieve; it is written as a function of the design variables. One or more goals can be involved in an optimization problem. The following is a mathematical representation of a multi-objective optimization problem,

$$F(x) = w_1 f_1(x) + w_2 f_2(x) + \cdots + w_n f_n(x) \; where \sum_{i=1}^{n} w_i = 1 \qquad 2.1$$

In this equation, w_i represents the weight constant whereas f_i represents the objective function.

A priori methods are used to make decisions before starting the optimization process. To indicate how important each objective is, weight set is required. The aggregation

of objectives enables single objective optimizers to find the global optimal solutions more efficiently. Although simple and computationally inexpensive, determining the assigned weight requires expertise. The a posteriori method refers to decision-making that occurs after an optimization procedure. There is no need to assign weights when using this method to find Pareto Fronts in a single run. However, it is more computationally expensive than the priori method. The optimization framework is shown in Figure 8. The system is treated as a black box by optimizer. It evaluates output and provides a set of inputs accordingly.

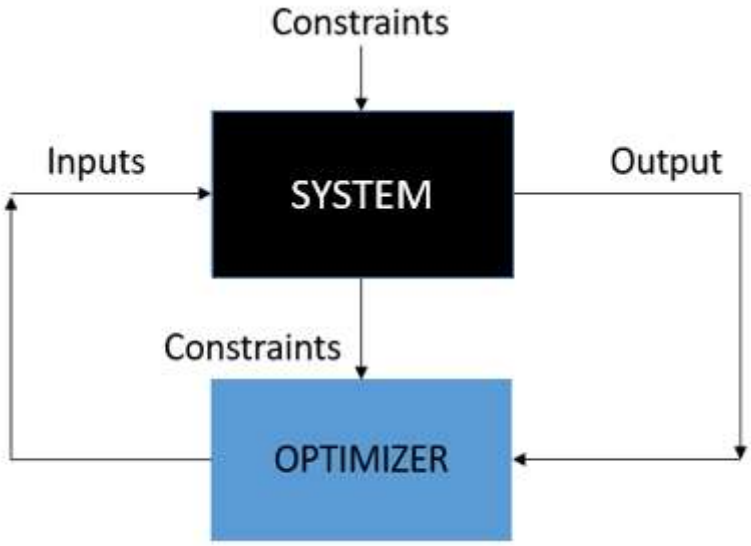

Figure 8. Optimization Framework

Turbomachinery design is a difficult task, because of the complicated flow inside and the thermal and structural issues that arise as a result of the flow passing through the blade passages and the rotation of the device. The typical trial-error design method, which mainly relies on the designers' experience, cannot provide globally optimum design [22]. As a result of automating the traditional design procedure and coupling an optimization method, the cost of the designer is reduced and the design process that depends more on a systematic approach rather than on designer experience is developed. An overview of turbomachinery aerodynamic design optimization is shown in Figure 9 which is reproduced from Ref. [22]. There are two types of turbomachinery aerodynamic design optimization techniques: inverse

designs and direct designs. In the case that the ideal turbomachinery shape is derived from the specified ideal flow conditions, the design method is known as inverse design. While the computational cost of the inverse design is inexpensive, designer understanding and experience are necessary to specify desired characteristics such as velocity or pressure. Direct design is utilized when the ideal objectives are determined by modifying the design variables. In a direct method, the input is the geometry and the output is the performance of the flow field. Gradient-based approaches and stochastic algorithms are two types of direct design. Gradient-based approaches rely on the objective function's local derivative. These techniques use the steepest descent method, conjugate gradient method, quasi-Newton techniques, or adjoint formulations to determine a search direction by beginning with a single design point and utilizing the local gradient of the objective function in relation to changes in the design variable. In these methods, first a design point is chosen and then the search direction is determined based on the local gradient of the objective function with respect to the change in the design variable. Provided that the objective function is convex and differentiable, these methods are effective and allow finding the optimum point. The optimization process, however, can occasionally produce a local optimum close to the initial point, instead of a global optimum [22]. Stochastic algorithms, search for global optimum rather than local optimum. Compared to gradient-based methods, stochastic algorithms are computationally expensive. Furthermore, the shape of the objective function is often complex due to the fact that the aerodynamic performance is not directly related to geometrical design parameters [9]. Simulated annealing (SA), particle swarm optimization (PSO), genetic algorithms (GAs), and evolutionary algorithms are all examples of popular stochastic optimization methods. Surrogate models are thus used to predict computationally expensive functions. In the field of turbomachinery design, some well-known models include the Artificial Neural Network (ANN), the Response Surface Method (RSM), and the Kriging Model. Surrogate models must be both cost-effective and accurate.

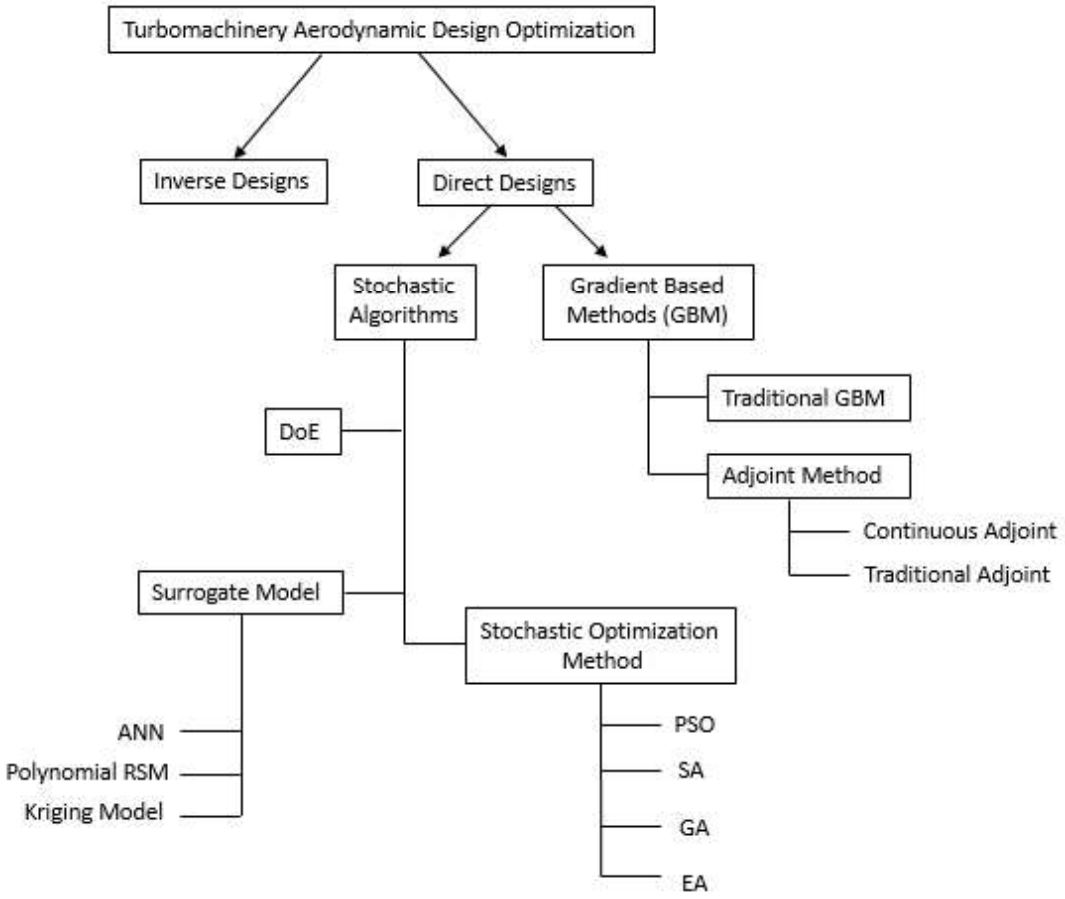

Figure 9. Turbomachinery aerodynamic design optimization overview (Produced from [22])

2.1 Design of Experiment

A minimum dataset of input and the corresponding output is required to construct a meta-model. To decrease the number of design calculations, which are computationally expensive, experimental designs attempt to give the most data with the fewest design experiments [22]. Since the cost of the experiment is significantly influenced by the quantity of data and the distribution of the points has an impact on the surrogate model prediction capacity, the design of the experiment should be selected by considering reducing the fitting error and time cost of the experiment [9]. Classical experimental designs include Central Composite Design (CCD), Factorial

Design, D-Optimal Design, and Box-Behnken Design. CCD is a five-level factorial design that is a good alternative to quadratic response surface approaches [23]. Several experiments are calculated using the 2^n+2n+1 equation, and point distributions consist of one center point others are mainly on edges and outside of the design space [24]. Many authors agreed that space-filling experimental designs should be used for deterministic computer analysis [25], [26]. The Latin Hypercube Design (LHD) sampling method is a gap-filling method that allows for widespread and fills the design space [25]. Furthermore, LHD estimates the mean, variances, and distribution functions of the output more precisely than random sampling. LHD is also less expensive and capable of dealing with a high number of input variables [22]. LHD is a matrix m x n order, where m represents the number of sampling points to be evaluated and n represents the number of design variables. Maximizing the reciprocal distance between samples in the decision variable space is a part of the optimal space-filling design, which ensures DoE's apparent efficacy is increased. LHD and Optimal Space Filling Design are compared in Figure 10. Optimal space filling is the optimization of LHD to better fill the parameter space. It evenly distributes the design parameters over the design space.

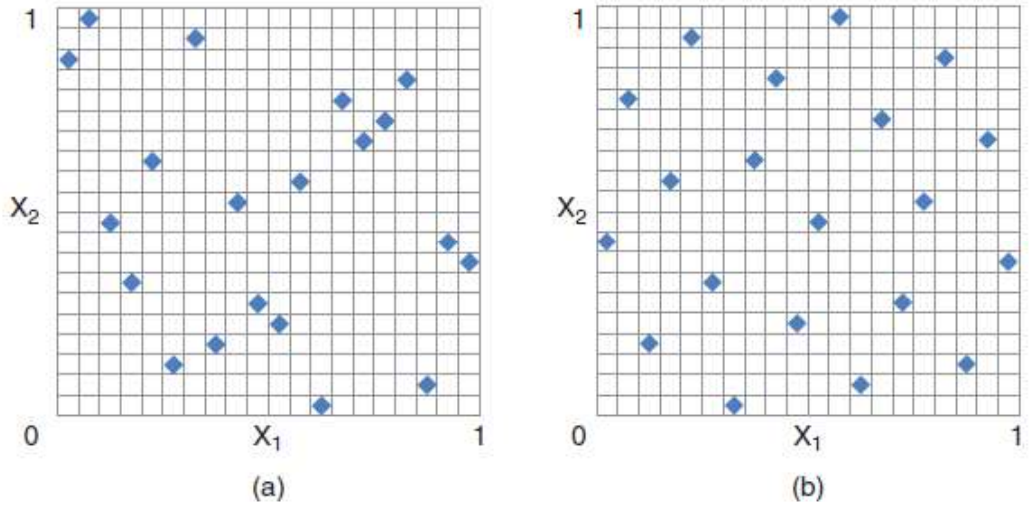

Figure 10. Comparison of LHD (a) and Optimal Space Filling Design (b) [23]

2.2 Surrogate Models

Surrogate models are used for replacing the real functions which are computationally expensive with reasonable predictions. Surrogate models, in other words, are low-fidelity models or merely approximation models. The low-fidelity model gathers data from the high-fidelity one in order to generate a solution quickly. Mostly used surrogate models are Polynomial Response Surface Model, Artificial Neural Network (ANN), and the Kriging Model.

The multilayer perceptron (MLP), Back Propagation Neural Network (BPNN), and the Radial Basis Function (RBF) are just a few examples of the many various kinds of ANN techniques. The most commonly used ANN technique is the Back Propagation Neural Network (BPNN). In this technique, the process starts with a small random values of the weight and bias factors. The input vector of the first training sample is then fed into the network, and the signal is then sent to the output layer. In most cases, during the forward training phase, the output vector produced by the network does not match the desired output vector connected to this input vector. Then, the difference between the real and desired output vectors is back-propagated to the network's input, and the difference is used to change the connection weights to reduce error. In the learning process, a set of input and output vectors are required to be successfully input to the network input and output layers. Until the weights converge, this process (i.e., presenting the input and output vectors to the network and updating the weights) is repeated for each training set [22]. Training a network with an RBNN takes significantly less time on the computer than with the more common BPNN. The RBNN has three layers: input, hidden, and output. These layers are composed of nodes and the nodes in each layer are connected to the nodes in the previous layer. The nodes in the input layer have the information of input variables and these are linked directly to the hidden layer without any weights, meaning that each hidden node receives the original form of input values. In the nodes of hidden layer, transfer functions, i.e., Radial Basis Functions (RBFs), are present. In multidimensional space, an RBF is symmetric around a mean or center

point. The output nodes are weighted in the second layer of connections, which are evaluated using a simple summation. The RBNN framework is given in Figure 11.

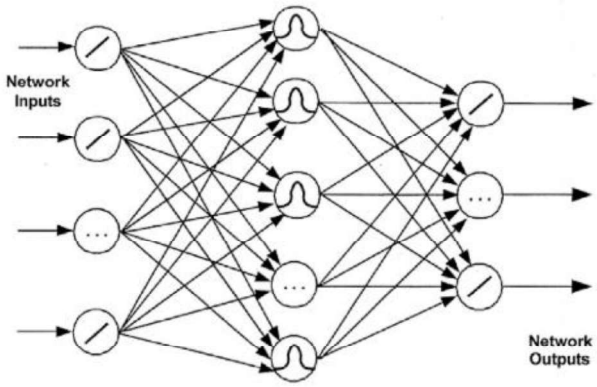

Figure 11. RBNN Structure [27]

Polynomial response surface methodology is another commonly used surrogate model. A response surface is a curve that best fits the data; it will be utilized in place of the data, as shown in Figure 12 [23]. The first step in RSM is to select a number of design points for the evaluation of the objective function, determination of which is computationally expensive. After looking into these points in depth, response surfaces are made to show how the design variables and the objective functions work together [22]. The most commonly used polynomial RSM method is a second-order function, which is given in Equation 2.1.

$$y = \beta_0 + \sum_{i=1}^{N} \beta_i x_i + \sum_{i=1}^{N} \beta_{ii} x_i^2 + \sum \sum_{i=1}^{N} \beta_{ij} x_i x_j + \varepsilon \qquad 2.1$$

where β is the regression coefficient, x the predictor variables and ε the total error [22].

As illustrated in Figure 12, second-order polynomial RSM has limited predictive capacity. The Kriging model fits the response surface from all design points. Due to the large number of correlation functions that can be used to construct approximation surfaces, they are adaptable. Thus, both linear and nonlinear functions are accurately

predicted by Kriging models. The Kriging model's strength lies in its ability to minimize the number of input parameters, which is especially helpful when working with a small database [22]. Kriging models are thought to give the most accurate predictions of all the possibilities, but they need a great deal of computing power to construct [28]. In contrast to polynomial RSM, Kriging utilizes a multidimensional interpolation that combines a polynomial model with local deviations. While the polynomial model models the design space globally, local functions are used for modeling the local deviations. The interpolation difference between Kriging and Polynomial RSM can be seen in Figure 12. The output function can be formulated as,

$$y(x) = f(x) + Z(x) \tag{2.2}$$

where f(x) is a second-order polynomial and Z(x) is a perturbation term.

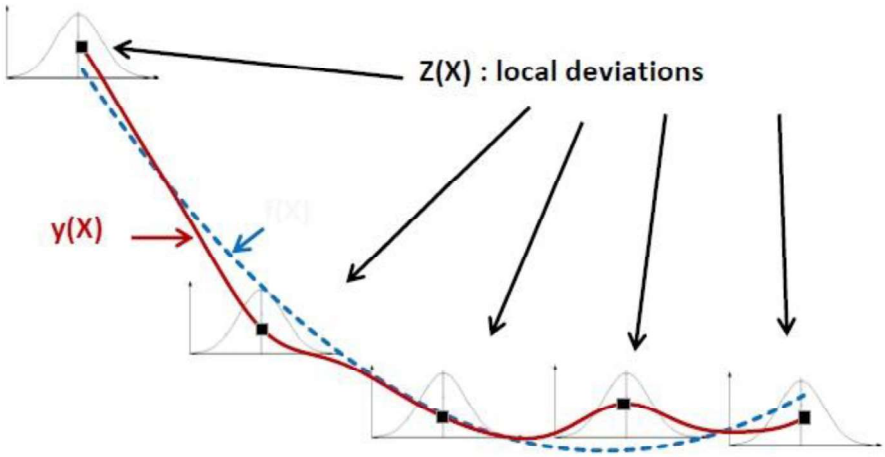

Figure 12. Kriging interpolation as compared to polynomial RSM (blue line represents second-order polynomial, red line represents Kriging) [23]

2.3 Optimization Algorithm

In this study, the centrifugal fan impeller is optimized using a Genetic Algorithm (GA) based on previous investigation in the literature [9], [15], [17]. Using Darwin's

evolutionary theory as a basis, the Genetic Algorithm attempts to optimize solutions. Figure 13 depicts a flow chart of the Genetic Algorithm, which is based on natural selection. A random population is used as a starting point for the Genetic Algorithm, which then iteratively improves upon that population. After a population is generated at random and the first generation is taken into account, objective functions or fitness values are determined. Using selection, crossover or recombination, and mutation as the main operators, we can generate new generations. Parents are selected from the general population based on their level of physical fitness. If you have higher fitness, you have a better chance of being picked by the selection operator. A roulette wheel or tournament selection is used to randomly select participants. Two parents are selected and then combined using the recombination operator to create offspring for the next generation. The first two operators, selection and crossover, involve the mixing of genes without producing any novel genes. It's possible that this would lead to less variety and the discovery of local optima. The mutation operator is applied to these issues by substituting a random number for a gene. Since the selection operator calls for a criterion to judge the quality of solutions, the GA algorithm can't handle problems with multiple objectives that have multiple best solutions. Accordingly, the GA algorithm needs to be adjusted so that it can effectively address problems with multiple objectives [29].

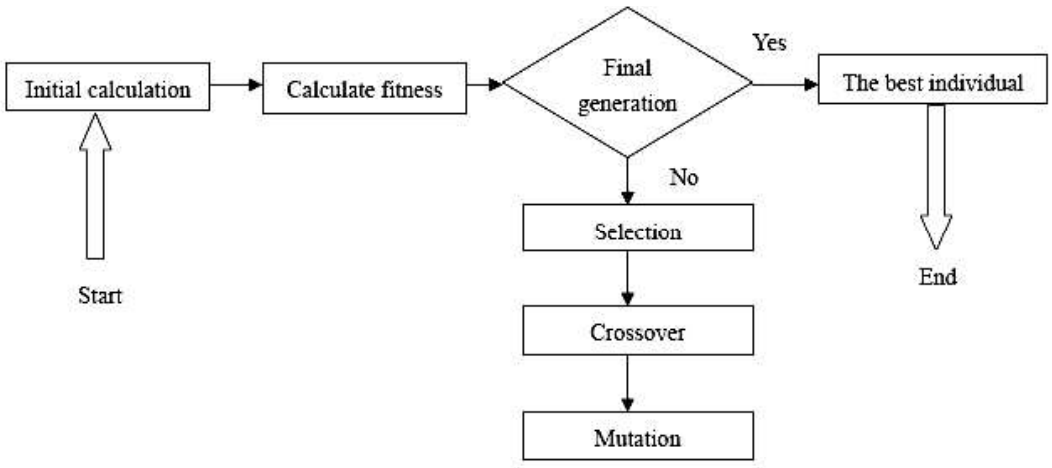

Figure 13. Flow Chart of Genetics Algorithm [9]

The Non-dominated Sorting Genetic Algorithm-II (NSGA-II) provides an efficient means of finding Pareto Optimal solutions in multi-objective optimization [30]. NSGA-II employs a fast nondominated sorting procedure, an elitist preserving strategy, and a parameterless niching strategy. The NSGA-II is intended to address the shortcomings of its predecessor, the NSGA. Non-dominated sorting genetic algorithm has many drawbacks, such as its high computational cost, lack of elitism, and the need to specify the sharing parameter. It is worth noting that even though the process time has decreased from $O(MN^3)$ to $O(MN^2)$, the storage requirements have increased from $O(N)$ to $O(N^2)$.

Each solution is compared to the other solutions in the population to find out which ones belong to the set of solutions on the first dominant surface. On the first dominant surface, this process is repeated for each solution. For the second dominant surface solution, the first-order solutions are discarded and start over. Therefore, individuals are categorized according to their level of dominance. For each of the p members of the P population, the dominance number and the dominant solution set are computed. The domination count for all solutions in the first nondominated front will be zero. Following that, it is compared to the other solutions. As a result, if member's domination count drops to zero, that member is moved to its own list, Q. These individuals are part of the second nondominated front. Next, we follow the same steps with the rest of the group to locate the third front. Once a front is identified, the procedure is repeated to find any others. The fast non-dominated sorting algorithm can be seen in Figure 14.

```
For each p ∈ P

  Sp=Ø                          a set of solutions that the solution p dominates
  np=0                          the number of solutions which dominate the solution p
  For each q ∈ P
          if (p≺q) then         if p dominates q
              Sp=Sp U {q}       Add q to the set of solutions dominated by q
          else if (q≺p) then    if q dominates p
              np=np+1
  if np=0 then                  no dominant solution to p, p belongs to the first front
          prank=1
          F1=F1 U {p}           First front is updated by adding solution p

i=1                             Initialize the front counter
while Fi ≠ Ø                    The process is repeated as long as the surface differs from the empty set.
  Q = Ø                         Used to store the members of the next front
  for each p ∈ Fi
          for each q ∈ Sp
              nq = nq -1
              if nq = 0 then    q belongs to the next front
                    qrank = i+1
                    Q = Q U {q}
  i = i+1
  Fi = Q
```

Figure 14. Fast non-dominated sorting algorithm [30], [31]

Another important approach of NSGA-II is crowded comparison, which is replaced by the sharing function of NSGA so that the Pareto solution set has dispersion and diversity of solutions. This new method keeps populations diverse without requiring the user to set any parameters. A rough estimate of the density of solutions in this region can be obtained by calculating the average distance along each objective between two points on either side of a solution in the population. An approximation of the perimeter of a cuboid whose vertices are points that are the next most distant neighbors is provided. The average side length of the cuboid shown in Figure 15 as a dashed box, is the crowding distance of the i_{th} solution in its front. The selection process is directed by the crowded distance comparison operator to evenly disperse the Pareto Optimal Front. As a result, if i_{rank} equals to j_{rank}, the solution is dominated by the higher crowded distance.

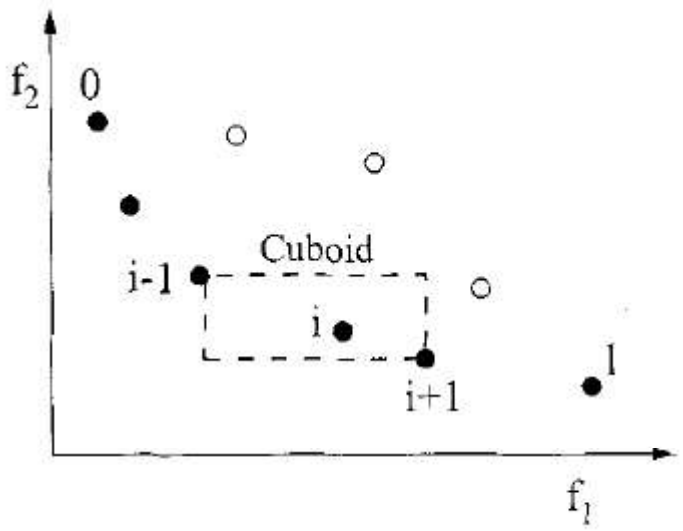

Figure 15. Crowded-distance for two objective functions [30]

Figure 16 depicts the NSGA-II procedure. Firstly, populations *P* and *Q* are combined to form population R_t. The new population R_t, which has a size of 2N, is ranked and sorted based on non-domination. In general, the population size would be greater than the number of solutions in all sets from F_1 to F_l. All solutions until F_l, $F_{l,}$ and F_2 in Figure 16, are direct members of P_{t+1}. To select exactly N population members, solutions of the last front, F_3 in Figure 16, is sorted in descending order using the crowded-comparison operator and the best solutions required to fill all population slots are selected. The new population P_{t+1} is now used for selection, crossover, and mutation, resulting in the creation of a new population Q_{t+1}.

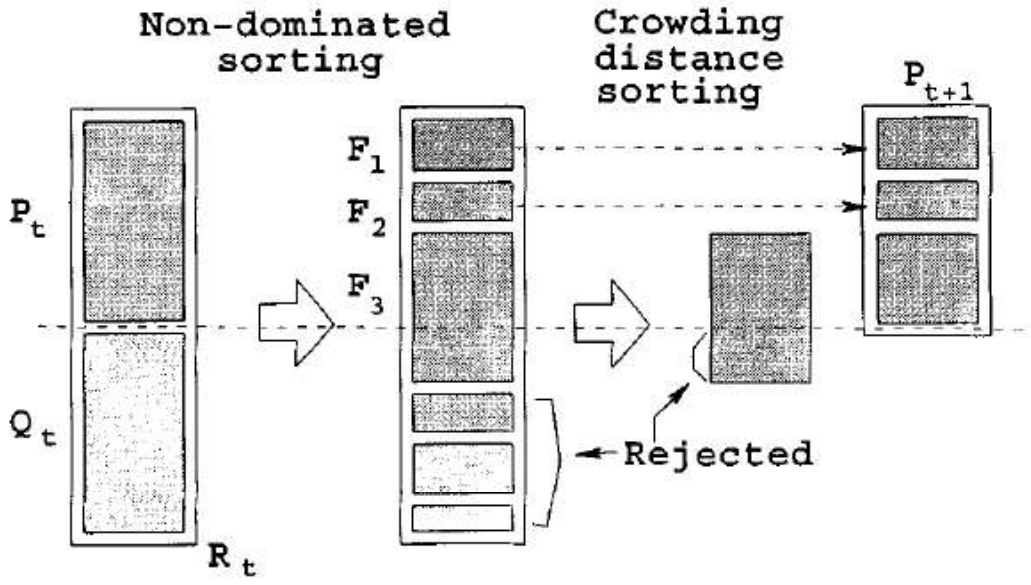

Figure 16. NSGA-II methodology [30]

CHAPTER 3

VALIDATION STUDY

In this part of the study, the experiment conducted by Hathaway et al. [32] is used to confirm the validity of the numerical model. In that study, the flow field of the NASA Low-Speed Centrifugal Compressor (LSCC) was experimentally investigated by the laser anemometry method. The experiments were performed in 1995, and since then, the results of the study have been used in many studies to assess the ability of the three-dimensional Navier-Stokes codes. Figure 17 shows a schematic diagram of the LSCC facility. The backswept impeller was equipped with a vaneless diffuser in the experimental setup. An air straightener was used to draw the room air into the plenum. A bell-mouth inlet with a contraction ratio of 10:1 was designed and utilized to create the inflow conditions specific to the compressor.

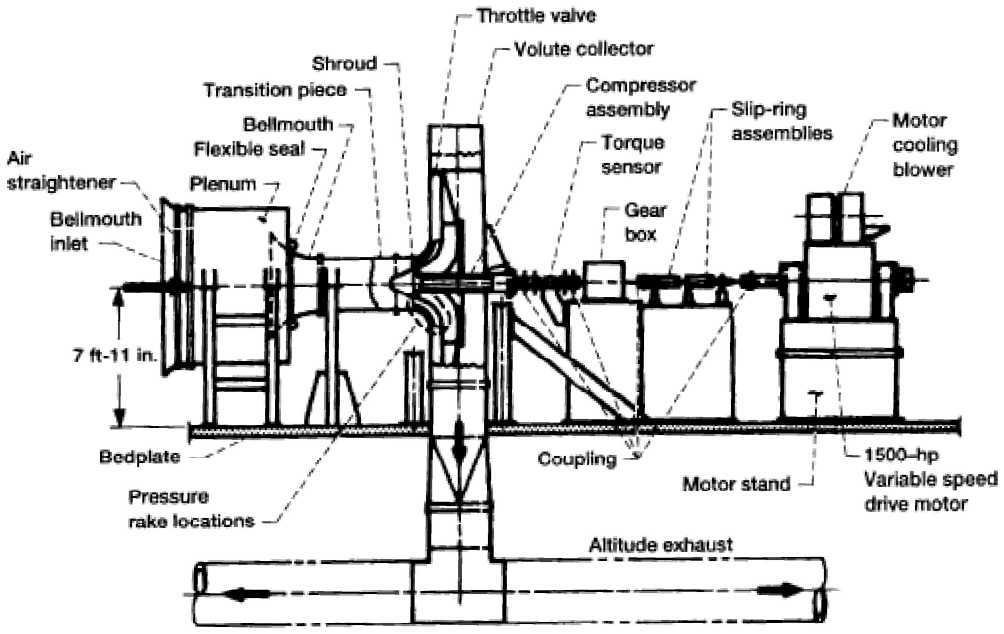

Figure 17. NASA Low-Speed Centrifugal Compressor (LSCC) experimental facility schematic diagram [32]

The three-dimensional velocity field was measured at several locations upstream, within, and downstream of the rotor in in Ref. [32]. At stations upstream and downstream of the rotor, span-wise pneumatic probe surveys of total and static pressures, total temperature, and flow yaw and pitch angles were also performed. Overall compressor performance was calculated using the probe survey data.

Figure 18 depicts the test impeller, which has a design tip speed of 153 m/s. A vaneless diffuser was positioned downstream of the impeller to create an axisymmetric outflow boundary condition, a type of boundary condition frequently employed in Computational Fluid Dynamics (CFD) analysis of isolated blade rows.

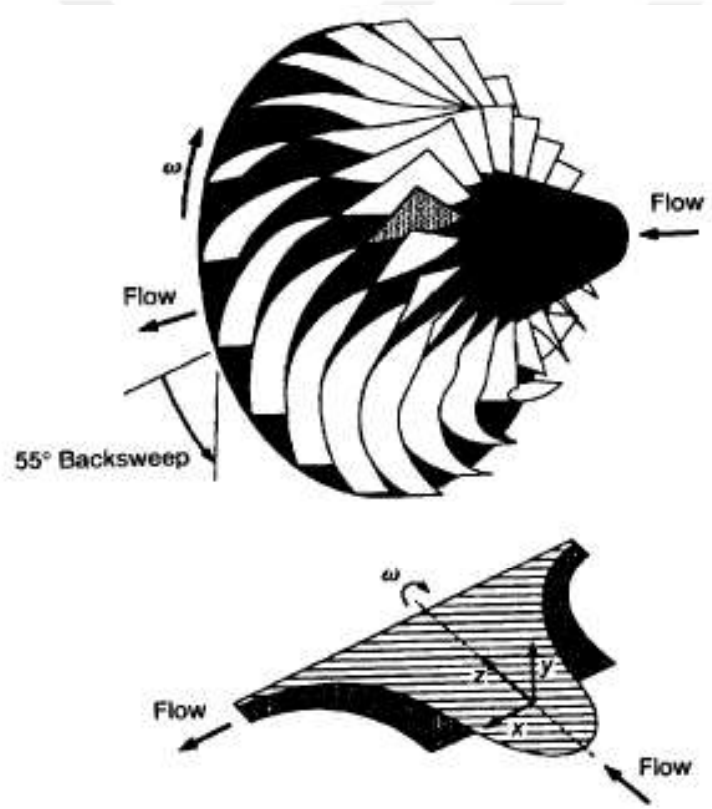

Figure 18. NASA LSCC Test Impeller [32]

Design parameters are given in Table 5. The impeller has 20 blades and a backsweep angle of 55°. The exit blade height is 0.141 m and the exit diameter is 1.524 m.

Table 5. NASA LSCC Impeller Blade Parameters. (Reproduced from [32])

Parameter	Value	Unit
Inlet total pressure, P_{t1}	Variable*	[Pa]
Inlet total temperature, T_{t1}	Variable*	[K]
Design Shaft speed, n	1862	[rev/min]
Design mass flow rate, m	30	[kg/s]
Number of blades	20	-
Backsweep from radial	55	[degree]
Pressure ratio of impeller	1.14	-
Impeller efficiency	92%	-

** Pressure and temperature values are provided throughout the span at the inlet of the impeller*

3.1 Generation of the impeller model

The impeller model is generated in two tools, i.e., BladeModeler, used for blade-modeling and TurboGrid, especially used for meshing, to assess the performance of both tools. In the BladeModeler, blade angle and thickness distributions of the LSCC impeller geometry, which can be seen in Figure 19, are prescribed, whereas in TurboGrid, hub, shroud, and blade profile curves are imported in order to the impeller model. BladeModeler also allows the designer to enable the hub fillet option and parametrize it. Then, the impeller fluid domain is created and meshed for further numerical calculations. For both approaches, the pressure ratio and the efficiency values are calculated and tabulated in Table 6. Since the two methods yield similar results, TurboGrid is selected for the generation of the impeller model in further analyses.

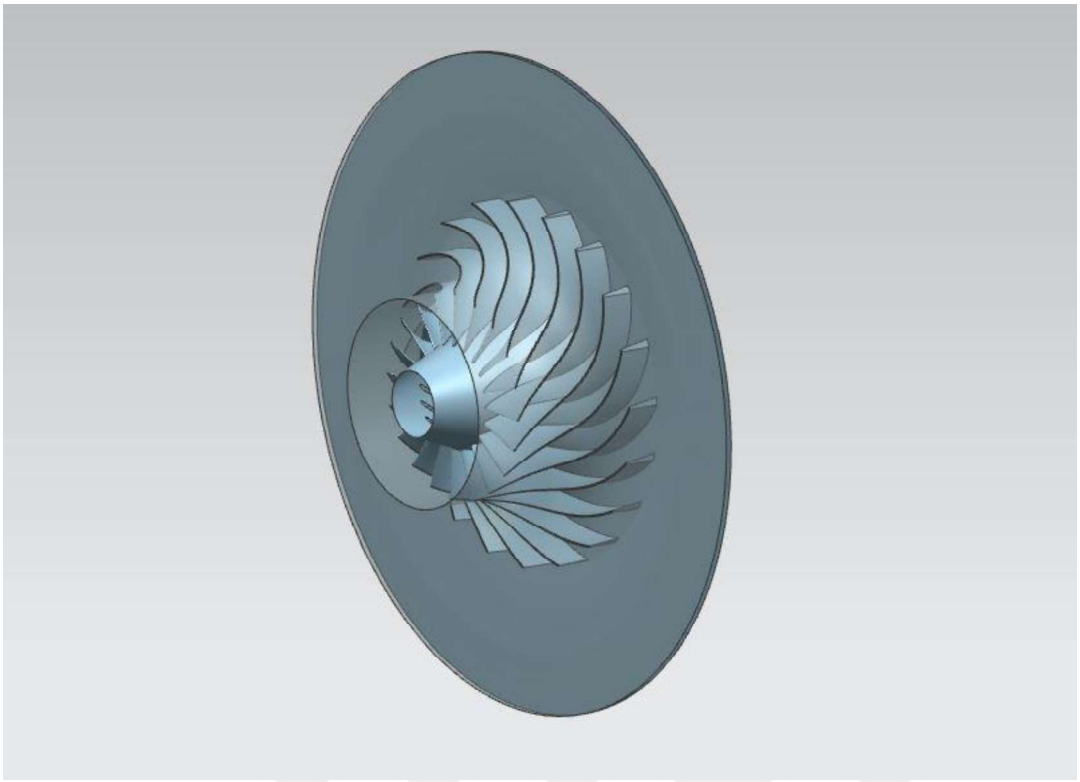

Figure 19. NASA LSCC impeller model created in Siemens NX

Table 6. Pressure ratio and efficiency calculations at the design point by using BladeModeler and TurboGrid

Tool	Pressure Ratio	Efficiency
BladeModeler	1.138	0.918
TurboGrid	1.139	0.938
Experiment	1.141	0.922

BladeModeler is a tool which provides the blade angle and thickness distributions; therefore, it is used for investigating our model blade angle and thickness distributions. Figure 20 and Figure 21 show the comparisons of the blade angle and thickness distributions of the model with those of the NASA LSCC [33]. A slight shift can be seen between the model and the original distributions of blade angle and thickness.

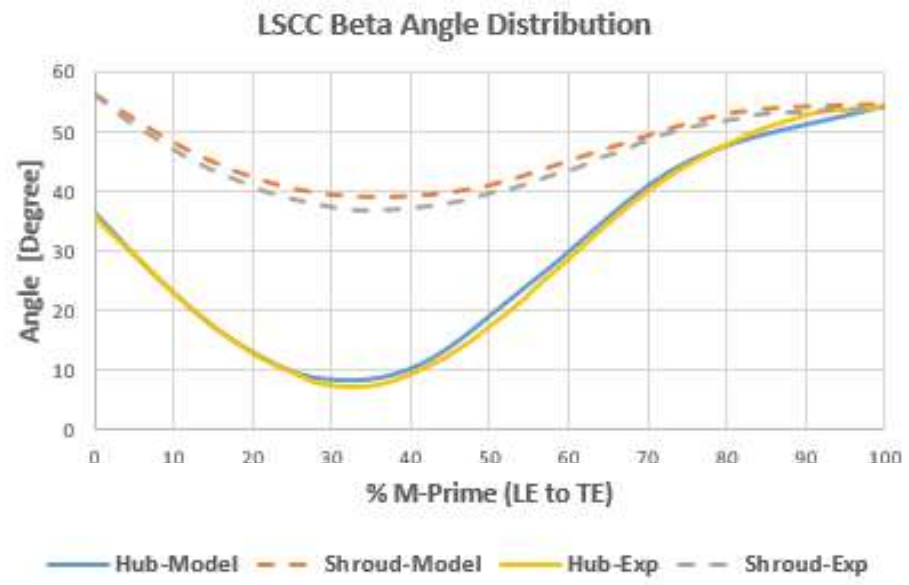

Figure 20. Beta angle distribution at the NASA LSCC impeller hub and shroud (yellow and gray lines) and the model (blue and red lines)

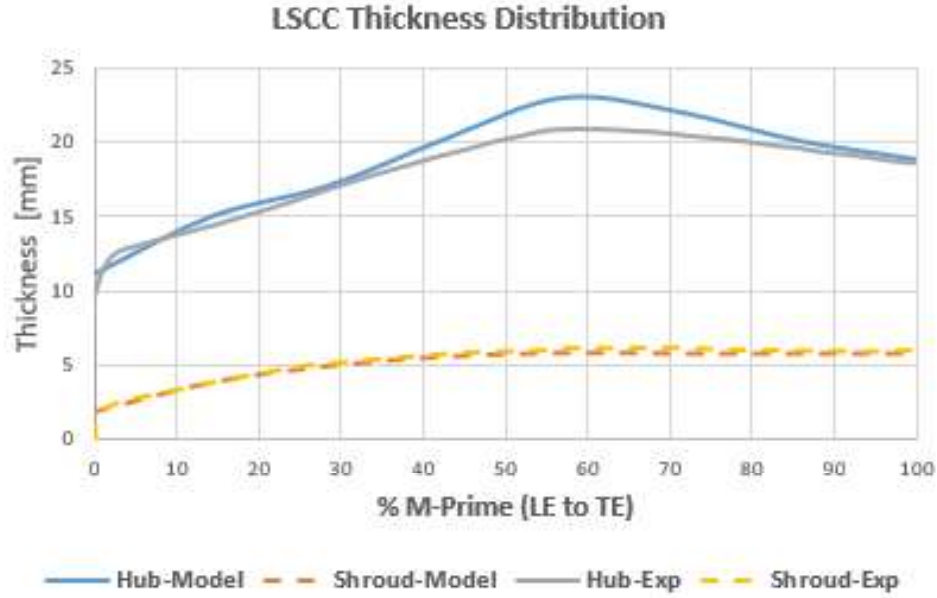

Figure 21. Thickness distribution at the NASA LSCC impeller hub and shroud (gray and yellow lines) and the model (blue and red lines)

3.2 Mesh Independence Study

Mesh independence study is carried out to determine the optimal number of grid points in the computational mesh. One flow passage of the 20-bladed impeller is modeled using a periodic boundary condition to shorten the computational time for CFD analyses. TurboGrid is used to generate an H-type mesh topology after the model is created. According to Denton [34], using an O-type mesh topology on the leading edge instead of an H-type reduces losses significantly. Accordingly, the leading edge is discretized with an O-type mesh topology. Furthermore, because an error on the leading edge will affect the overall result, the leading edge's local mesh has been improved by increasing edge refinement [34]. In the mesh independence study, k−ω Shear Stress Transport (SST) and Spalart Allmaras (SA) turbulence models are used. The pressure ratio and total isentropic efficiency values obtained from the mesh independence study are shown in Figure 22 and Figure 23, respectively.

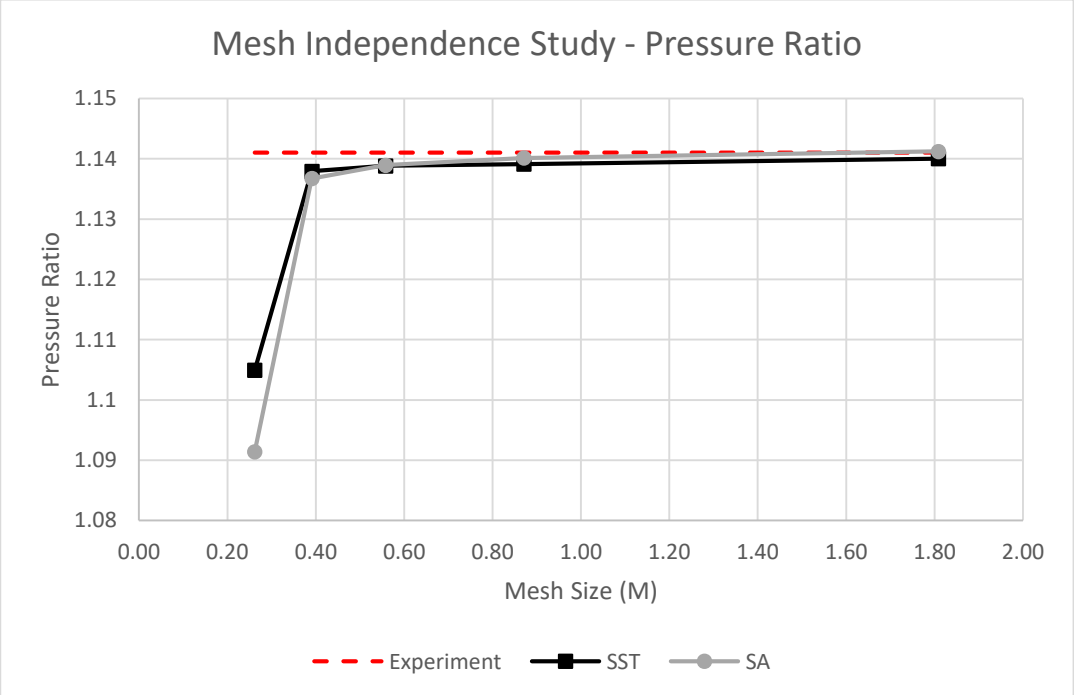

Figure 22. Mesh independence study based on the pressure ratio at the design point by NASA LSCC

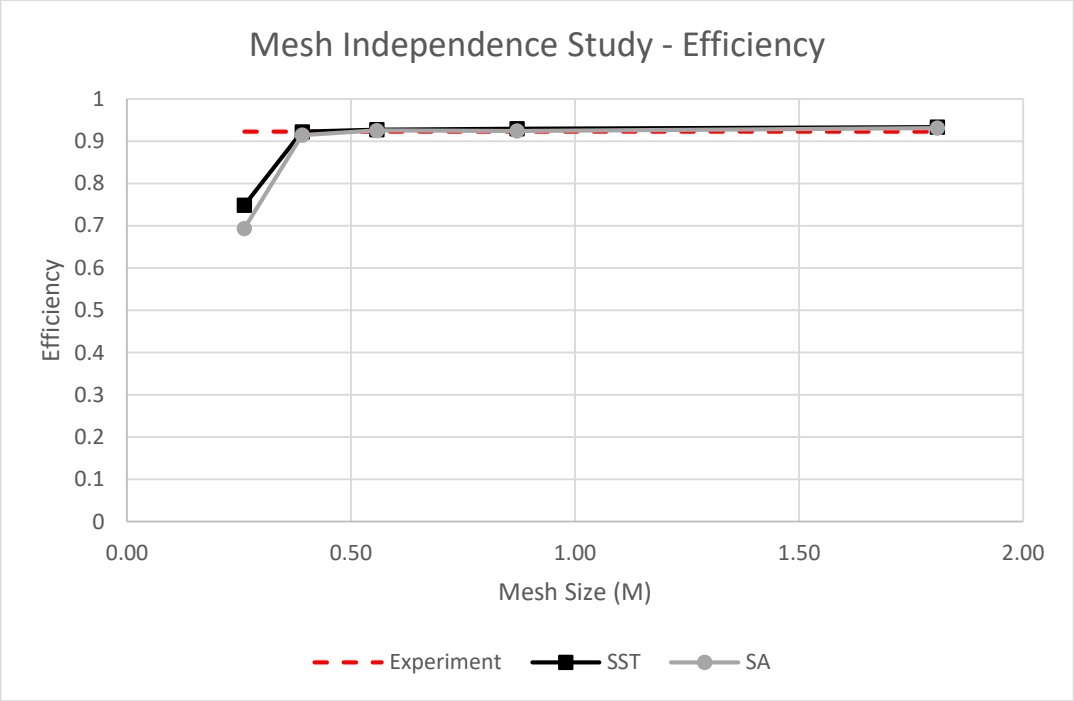

Figure 23. Mesh independence study based on the efficiency at the design point by NASA LSCC

Table 7 shows the passage, outlet, and entire domain mesh size. According to the results of the mesh independence simulations, the computational mesh with 0.4M grid points provides sufficient accuracy, which is consistent with the studies that have been published [34], [35]. In order to shorten the computation time for the optimization study, a computational mesh with 0.4M grid points is chosen. TurboGrid specifications for the selected mesh geometry and the mesh structure are given in Table 8 and Figure 24, respectively.

Table 7. Mesh Independence Study Results

Mesh Size (Elements/Millions)		k-w SST			SA		
Passage	All Domains	PR	TR	Efficiency	PR	TR	Efficiency
0.11	0.26	1.105	1.039	0.748	1.091	1.037	0.693
0.17	0.39	1.138	1.039	0.922	1.137	1.041	0.914
0.26	0.56	1.139	1.041	0.927	1.139	1.041	0.925
0.44	0.87	1.139	1.041	0.929	1.140	1.041	0.924
0.83	1.81	1.140	1.041	0.933	1.141	1.041	0.931

Table 8. Validation Case TurboGrid Specifications

TurboGrid Specifications	
Target Passage Mesh Size	400000
First Element Offset [m]	3.E-06
Constant First Element Offset	Enabled
Cutoff Edge Split Factor	1
Target Maximum Expansion Ratio Rate	1.3
Spanwise Blade Distribution Parameter Method	Proportional
Shroud Tip - Uniform	10
Outlet Expansion Rate	1.1
Limit Aspect Ratio Request Max AR-900	Enabled
Total Nodes	920145
Total Elements	870860

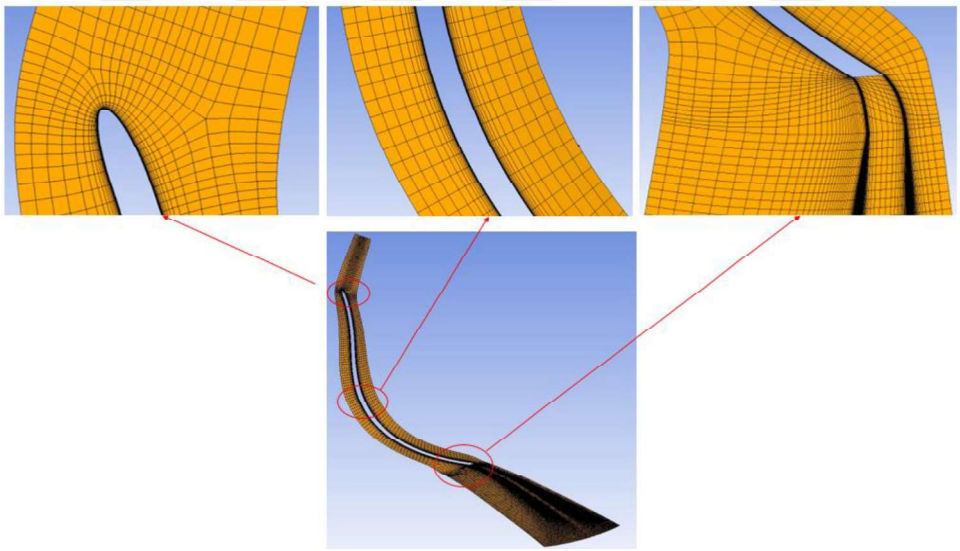

Figure 24. Detailed view of the 0.87M element mesh structure created with TurboGrid

3.3 CFD Solver and the Turbulence Model

The three-dimensional flow in the NASA LSCC flow is simulated using the ANSYS CFX under steady-state conditions. The simulations are also performed in the commercial StarCCM+ software to provide additional comparisons regarding the numerical solver. The working fluid is air, which is defined as an ideal gas. As inlet

and outlet BCs, the total pressure and the mass flow rate are provided, respectively. Other boundary conditions are specified as no-slip walls, excluding the blade shroud, which is defined as a counter-rotating wall. A second-order accurate high-resolution method is used to solve the convection-diffusion equations. The flow field consists of two regions (rotating and stationary) and an interface, as shown in Figure 25. The interface employs the frozen rotor method. According to the experiments, the tip clearance is 0.254 cm [32].

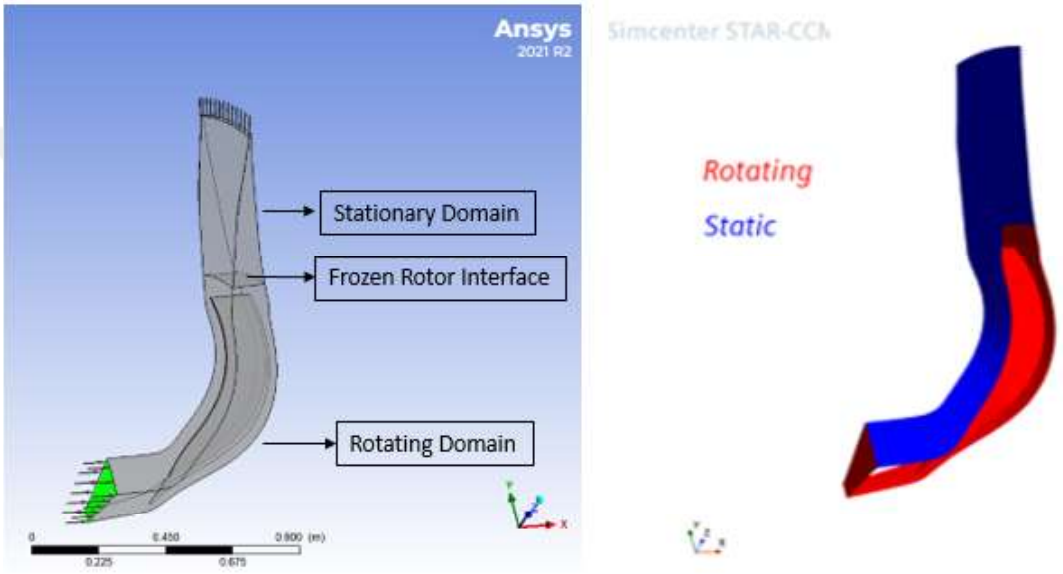

Figure 25. NASA LSCC Flow Field Domain

Processes in which the mesh topology needs to be changed automatically, such as compressor geometry optimization, require robust turbulence models that can deal with different mesh topologies and reduce failed solutions [36]. Hence, $k-\omega$ SST and SA models are used for the turbulence closure. The $k-\omega$ model uses a blending function in the SST model which provides a seamless transition between two models; a $k-\omega$ model at the near-wall region and the k–ε model in the bulk region. Moreover, the treatment of near-wall effects in turbulence modeling is crucial since near-wall formulation governs the precision of the wall shear stress. To fully solve the near wall region, the y+ value less than one is aimed, which corresponds to a first cell

height of 3x10-6 m. The y+ contours of both CFX and Star CCM+ solvers are shown in Figure 26.

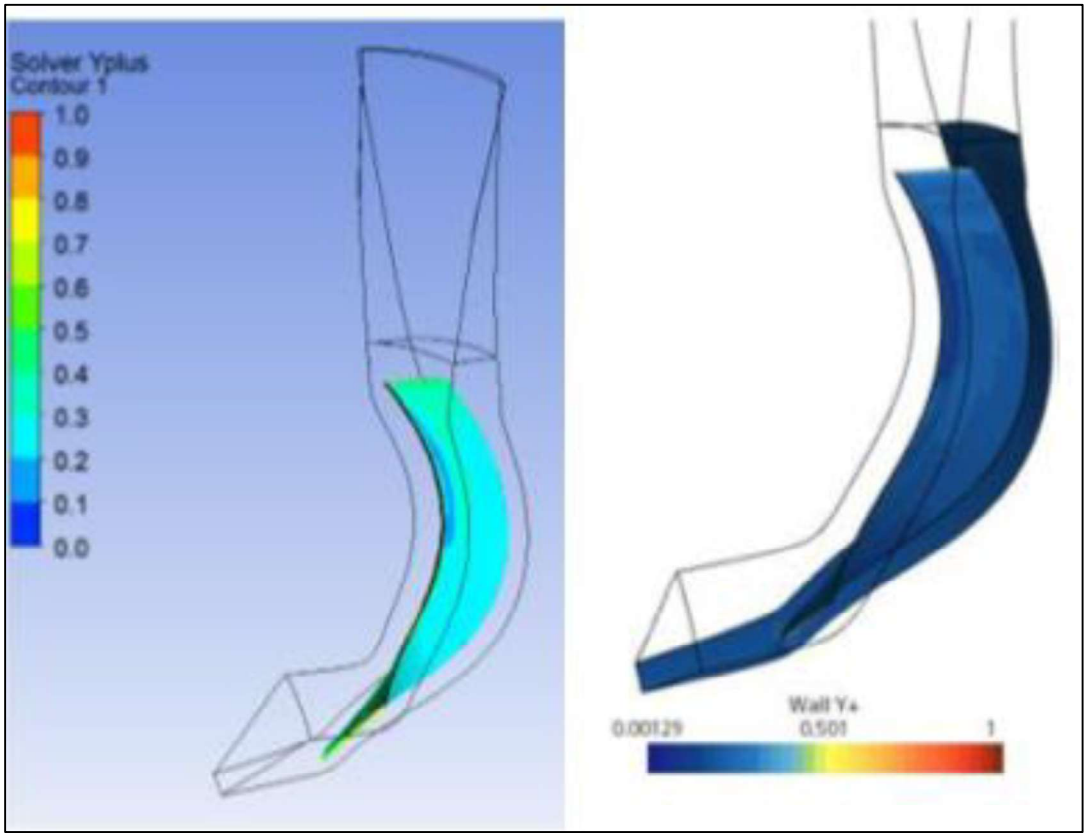

Figure 26. y+ contours belong to CFX (left) and Star CCM+ (right)

Figure 27 compares the performance curves generated by numerical analyses in CFX and Star CCM+ to the NASA LSCC experimental data. The figure demonstrates that the results of the simulations with $k-\omega$ SST and SA turbulence models are very close to the results of the experiments. During the experiment [37], audible unstable flow conditions are recorded at flow rates of less than 20 kg/s. As mentioned by Bourabia et al. [38], an unsteady analysis should be preferred to provide more accurate results where the flow rate is less than 20 kg/s.

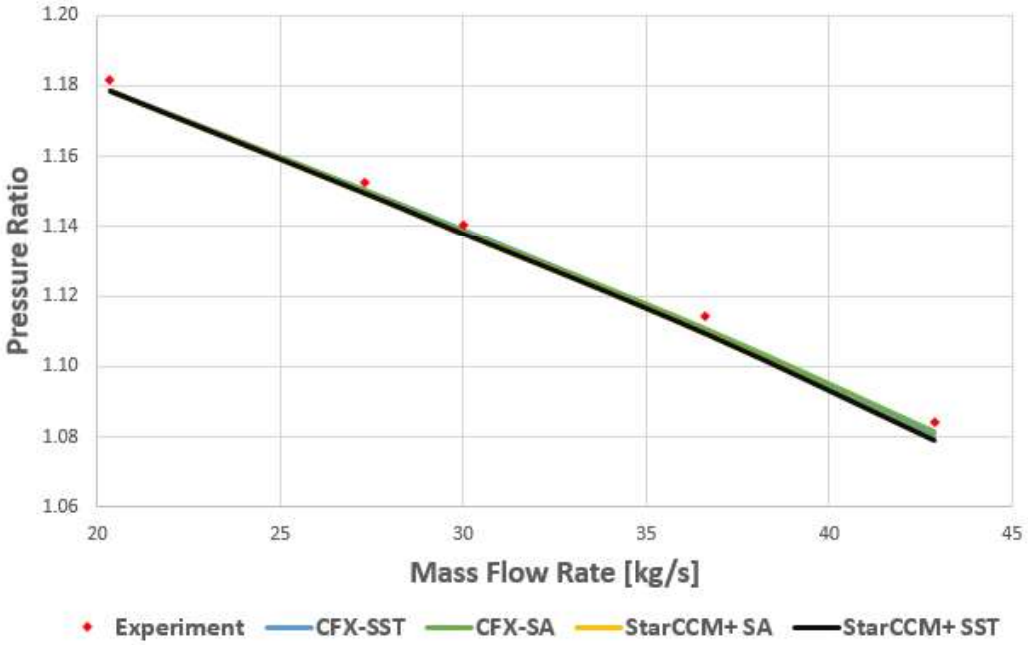

Figure 27. NASA LSCC performance curve [32] and the comparison of the performance of two different turbulence models ($k-\omega$ SST and SA) and two different commercial tools (ANSYS CFX ve StarCCM+) on the prediction of the performance curve of NASA LSCC

As a result, the CFX with the turbulence model $k-\omega$ SST is selected to be used in the optimization due to its performance in the calculation of the pressure ratio. It should be noted that ANSYS Workbench Environment, which includes tools for geometry, meshing, CFD analysis, and design exploration, provides an integrated and automated optimization workflow in this manner.

CHAPTER 4

APPLICATIONS AND EVALUATIONS

4.1 1D Centrifugal Fan Impeller Preliminary Design

Since the entire design process is based on simultaneous experimental or numerical analyzes, the required time and cost are high, and such studies are considered inefficient. Preliminary design studies are now carried out, which comprise the start of the impeller design utilizing the experimental data (correlations) available in the literature. Many commercial software packages are utilized in preliminary design research. The low-fidelity techniques used by all of these commercial software are based on experimental correlations and aerothermodynamics relations. Vista CCD was utilized in the preliminary design phase of this study because of the wide range of design parameters that may be fed into the software [38].

Efficient fan design starts with the selection of a fan type, which is primarily based on the Cordier diagram, which is a measurement-based empirical diagram. It establishes a connection between the four variables of flow rate Q *(m^3/s)*, pressure P *(Pa)*, rotating speed ω *(rad/s)*, and diameter D *(m)*. It is dependent on speed number σ and diameter number δ.

$$\sigma = \frac{\omega * \sqrt{Q}}{\left(\frac{\Delta P}{\rho}\right)^{0.75}} \tag{4.1}$$

$$\delta = \frac{D * \left(\frac{\Delta P}{\rho}\right)^{1/4}}{\sqrt{Q}} \tag{4.2}$$

As seen in Figure 28, a fan that has a specific speed greater than two is more suitable to be in axial configuration, whereas specific speed less than 0.4 stands for a radial

flow. In between these values, a diagonal (mixed) flow fan should be selected. Since provided drive shaft for the oil cooler fan is vertical, the installation is the main criterion driving the fan type selection. For the oil cooler fan, the expected requirements are specified as follows;

Table 9. Oil Cooler Fan Expected Requirements

Parameter	**Value**
Mass Flow Rate [kg/s]	0.9
Pressure Rise [Pa]	7100
Rotational Speed [rpm]	9000
Max Operating Temperature[1] [^{o}C]	110
Max Power @110 ^{o}C [kw]	15

Note 1: Maximum oil temperature is 110 ^{o}C and the centrifugal fan is placed downward of the heat exchanger, the maximum fan air inlet is assumed 110 ^{o}C.

When customer requirements are inserted in equation 1, the speed number is found 1.14 which indicates for diagonal (mixed) type. Because centrifugal fans increase air temperature at the exit, it is best to install them downstream of the oil cooler heat exchanger to maximize heat exchanger efficiency. Outside ram air is directly supplied to the oil cooler as a result of this design. It is also preferable to direct exhaust air from fans to the atmosphere. Given the installation and structural constraints, it is required to design a centrifugal fan for the oil cooler which has vertical drive shaft.

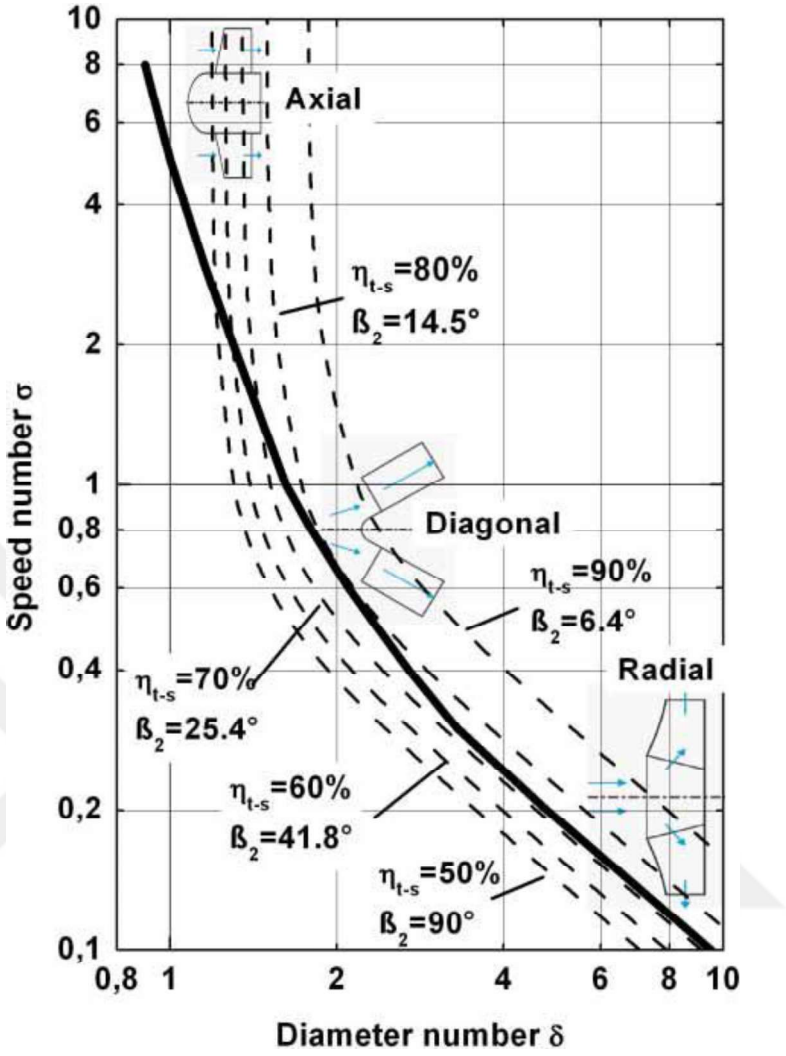

Figure 28. Cordier Diagram [39]

There are some important parameters provided in the 1D design phase. Some of these are, diffusion ratio, meridional velocity gradient, incidence angle, tip clearance, impeller inlet and outlet angles.

The establishment of an appropriate diffusion ratio is one of the key principles for the aerodynamic design of impellers. The relative Mach number ratio, the relative velocity ratio, or the diffusion factor can be used to represent the impeller's diffusion [40]. In the literature, diffusion is expressed as either the Lieblein diffusion factor or the De-Haller number. The Lieblein diffusion factor, which is given in Equation 4.3, is concerned with diffusion along a blade surface [41]. In the study by Lieblein et al.

[42], the total pressure loss coefficient gradually increases until a diffusion factor of about 0.6, at which point the loss rapidly increases.

$$DF = \frac{w_{max} - w_2}{w_1} \tag{4.3}$$

The De-Haller number is the ratio of the relative velocity at the outlet to that at the inlet. In contrast to the Lieblein diffusion factor, it is concerned with diffusion on end walls [41], and it is defined in Equation 4.4.

$$DH = \frac{w_2}{w_1} \tag{4.4}$$

For the radial fans and pumps, a local diffusion factor may be used as well. It is defined in Equation 4.5. This factor should be limited to approximately 0.5 to avoid flow separation [43].

$$DF_{loc} = \frac{w_{max} - w_2}{w_{max}} \tag{4.5}$$

It can be seen in Equation 4.6 that the higher the diffusion factor is the more fan pressurizes the fluid. However, it should be selected to limit pressure losses and avoid flow separation.

$$\Delta P_t = \frac{\rho}{2}[(u_2^2 - u_1^2) + (w_1^2 - w_2^2)] + \frac{\rho}{2}(c_2^2 - c_1^2) \tag{4.6}$$

Another crucial factor is the inlet incidence which influences the operating range and efficiency, as shown in Figure 29. It is reported that the impeller incidence angle is typically set to almost zero at the design conditions [40]. Casey et al. stated thin compressor blades with a higher subsonic inlet Mach number may have an incidence range ±5°.

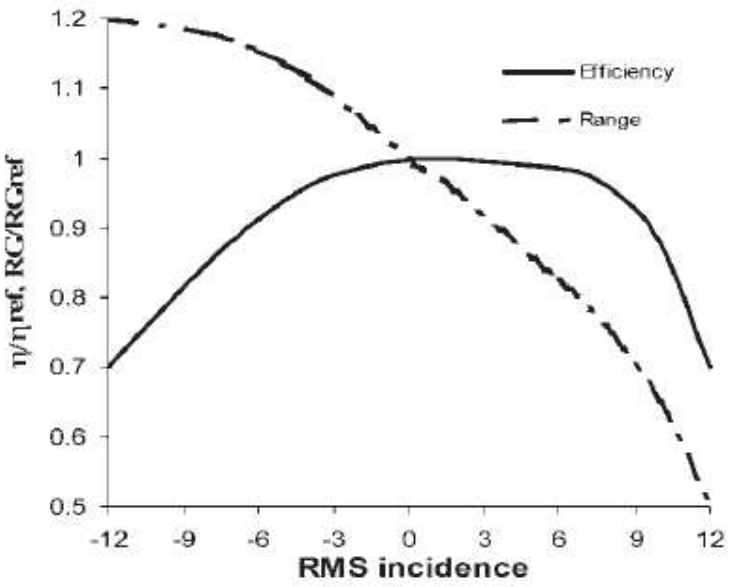

Figure 29. Influence of incidence angle on efficiency and operating range [40]

Another essential consideration is tip clearance. It has an effect on performance because it expands secondary flows within the impeller blades and creates intense tip vortices [40]. When tip clearance size is increased, efficiency declines and the stall margin deteriorates considerably [41]. The tip clearance in this investigation is set to 1 mm. Therefore, tip clearance ratio (tip clearance to blade height), is 0.014% for the leading edge and 0.021% for the trailing edge.

Shrouded and unshrouded impellers are the two common forms. The flow velocity around the casing of unshrouded impellers is very low at the inlet and increases near the exit. The velocity relative to the shroud for shrouded impellers is comparable to the velocity relative to the blade surface. As a result, shrouded impellers are frequently more efficient than unshrouded impellers [40].

Diffusers are used to transform kinetic energy into static pressure rise at the rotor exit. Vaned or vaneless are the types of diffusers that are used with centrifugal impellers. In this study, a vaneless diffuser is used. As stated by Lakshminarayana [44], Abdelhamid and Bertrand (1979) conducted experiments with and without a vaneless diffuser in a basic blower. The data were collected without a diffuser, with

the flow discharging into a room. It is discovered that the flow was stable without the diffuser and that the pressure rise improved significantly with the inclusion of a diffuser. However, the inclusion of the diffuser caused unsteadiness. It is the static pressure recovery coefficient, which gives the increase in static pressure between the diffuser's intake and its exit relative to the change in dynamic pressure at the inlet, that is the most important design parameter for evaluating the diffuser's performance. The pressure recovery coefficient, which is a measure of how much of the kinetic energy input into the diffuser is transformed into a static pressure increase at the diffuser outlet, is calculated using Equation 4.7 [41].

$$C_p = \frac{P_2 - P_1}{P_{t1} - P_1} \tag{4.7}$$

For the centrifugal fan, the optimum blade angle at the entry is found to be about 35º [45]. It is recommended that the rake angle of the trailing edge should be less than 45º [46]. It is recommended to have a backsweep angle, in the range of 20° to 55° [41]. The rake angle, backsweep angle, and shroud vane inlet angle are selected as default values of 30º and 45º and 60º, respectively. The rake and backsweep angle representation are given in Figure 30.

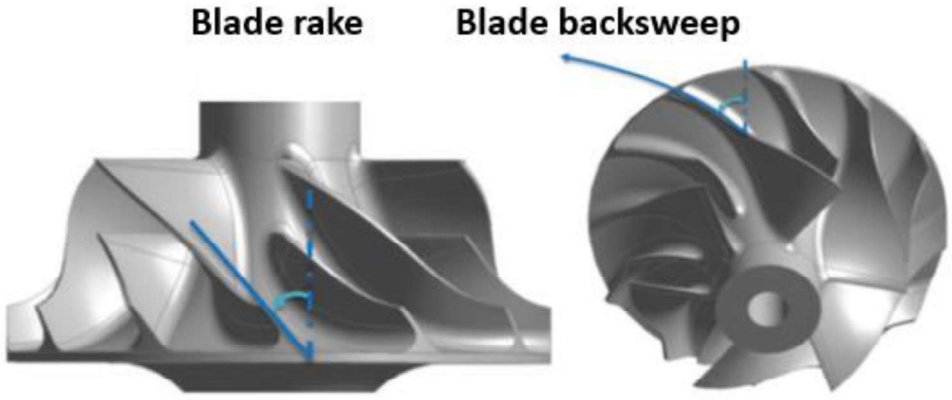

Figure 30 a) Blade rake b) Blade backsweep angle [47]

The flow coefficient of different turbomachines with respect to polytropic efficiency is given in Figure 31. As can be seen, Bommes – centrifugal fans have maximum polytropic efficiency between 0.07 and 0.10, which are the region for the high-

efficiency fans. Therefore, it is expected to design centrifugal fans in this flow coefficient range. It is also recommended to have a blade loading coefficient between 0.6 and 0.65 [41].

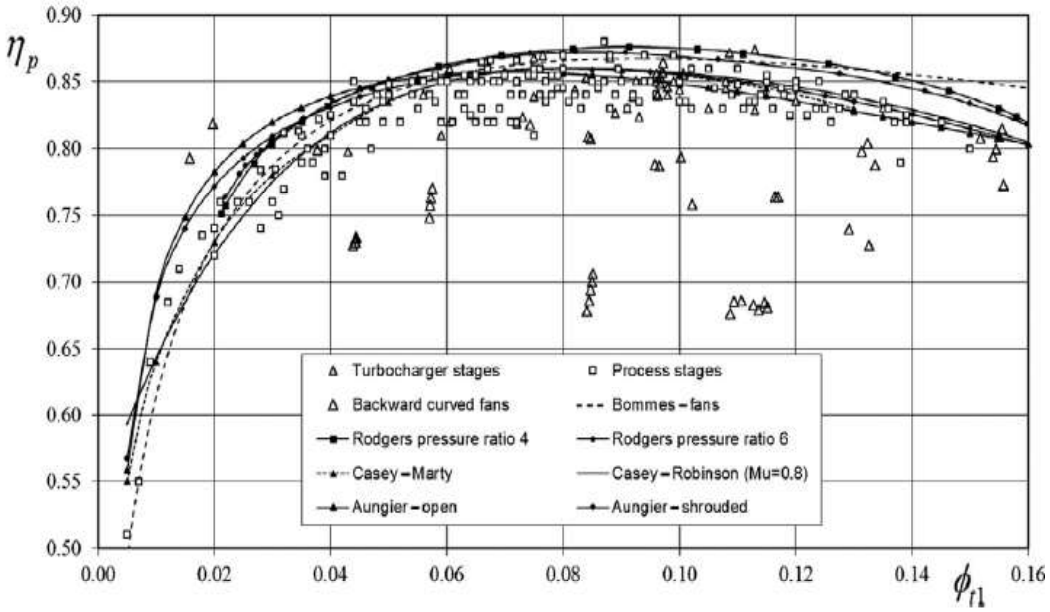

Figure 31. Polytropic efficiency versus flow coefficient (courtesy of Cambridge University Press) [41]

The geometric envelope and performance level are determined by one-dimensional (1D) design, which is one of the most crucial points in the design period. Since 1D design impacts the entire design process and a potentially incorrect design may not be corrected in the proceeding optimization study, it is crucial to have a reliable 1D design at the beginning of the process. Therefore, an optimization study for the 1D design is conducted. For the 1D design optimization reference parameters, and design space are given in Table 10.

Table 10. 1D design reference parameters and design space

Parameters	Lower Bound	Reference	Upper Bound
Relative Velocity Ratio	0.4	0.52	0.6
Incidence at shroud	0°	1.5°	3°
Inlet Blade Angle	30°	35°	60°
Backsweep Angle	20°	45°	55°
Blade Number	11	13	15

Maximizing static pressure and impeller isentropic efficiency are selected as objectives in the 1D optimization study. Moreover, Table 11 shows the constraints used in the 1D optimization study and their range.

Table 11. 1D optimization constraints and their range

$0.08 \leq \text{Flow coefficient} \leq 0.10$
$0.60 \leq \text{Blade Loading} \leq 0.65$

The parameters as input to the VistaCCD software for the 1D design and the values of these parameters are given in Table 12. The 1D preliminary design values obtained as a result of the analysis are tabulated in Table 13.

Table 12. 1D preliminary design specifications for the centrifugal fan impeller

Parameter	**Value**	**Parameter**	**Value**
Total pressure ratio	1.08	Hub Diameter	30 mm
Mass flow rate	0.9 kg/s	Vane inlet angle	58°
Rotational speed	9000 rpm	Tip Clearance	1 mm
Inlet temperature	383.15 K	Blades Number	11
Meridional velocity gradient	1.15	Backsweep	55°
Relative velocity ratio	0.58	Rake angle	30°
Incidence at shroud	1.74°	LE location on shroud [%M]	0

Table 13. The values of the impeller parameters obtained as a result of the 1D preliminary design optimization

Parameter	Value
Impeller exit diameter [mm]	276
Impeller exit height [mm]	47
Impeller Inlet height [mm]	75.52
Peripheral Velocity [m/s]	130
Tip Mach number	0.332
Power [kW]	9.52
Isentropic Efficiency	0.81
Flow Coefficient	0.098
Blade Loading	0.624

4.2 Parametrization

Parametrization is one of the significant parts of the optimization procedure. Radial impeller geometry is typically defined by the parametrized meridional contour at the hub and shroud (Figure 32a), and the blade camber line by the distribution of the angle β between the meridional plane and the blade camber line (Figure 32b).

Third-order polynomials are used to define the distributions at the hub and shroud [48]:

$$\beta(m) = \beta_{LE}(1-m)^3 + 3\beta_1 m(1-m)^2 + 3\beta_2 m^2(1-m) + \beta_{TE}m^3 \qquad 4.8$$

where m stands for non-dimensional meridional length. Leading edge and trailing edge angles are denoted by β_{LE} and β_{TE}, respectively. Then, the camber line circumferential angle θ from LE to TE, which is obtained using Equation 4.1, can be seen in Figure 32b.

$$Rd\theta = dm tan\beta \qquad 4.9$$

where R denotes the radius and dm denotes the differential meridional length.

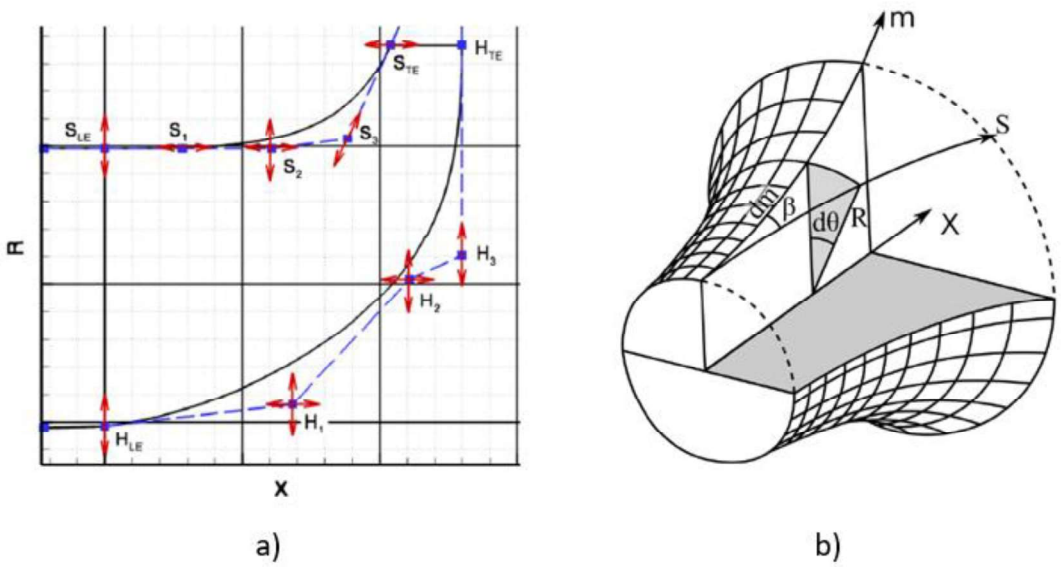

Figure 32. a) Meridional contour defined by Bezier control points b) Definition of the blade camber line by β angle [48]

The baseline blade angle distribution can be seen in Figure 33.

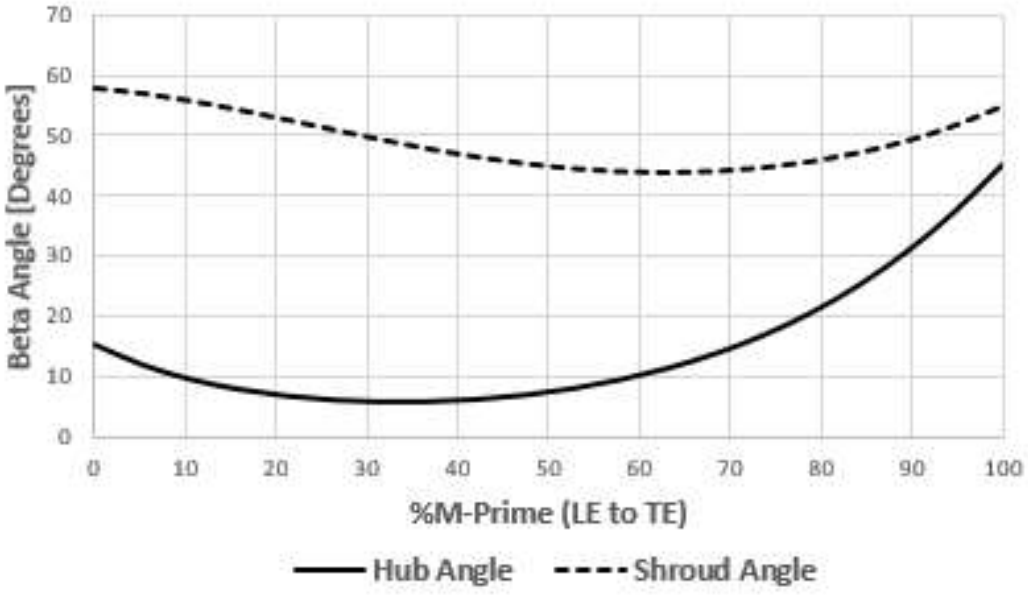

Figure 33. Baseline set blade angle (beta) distribution

According to the statement in the study conducted by Bamberger et al. [49], blade thickness is often chosen for structural factors and has little bearing on aerodynamic

performance. Additionally, since the thickness is one of the manufacturing limitations, during the optimization phase, the blade thickness is not selected as an optimization parameter.

Aerodynamic efficiency is increased and boundary layer losses are decreased by modeling the leading edge of the blades with an elliptical ratio of 4:1 at the hub and shroud, while the trailing edge is kept cut off [50].

Since this study mainly focuses on size optimization, impeller size is parametrized.

4.3 Baseline Design CFD Analysis

To observe the effect of 1D design optimization, two centrifugal impellers are designed, and an optimization study is performed on one of them. The other baseline design is based on the 1D design with reference values as stated in Table 10. Isometric 3D view of the 1D optimized baseline impeller can be seen in Figure 34.

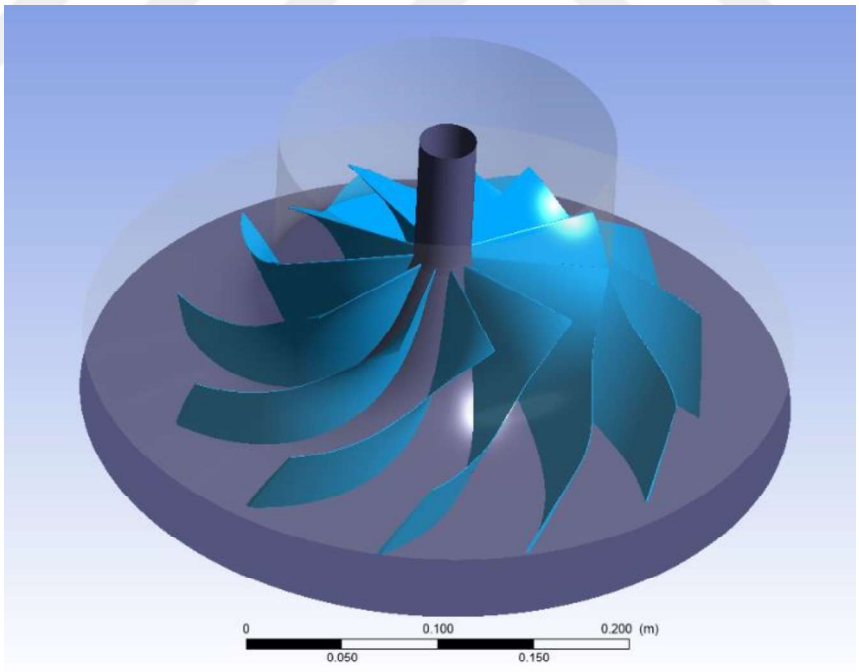

Figure 34. 1D Optimized baseline impeller 3D view

Volumetric flow rate versus fan static pressure and total to static efficiency graphs of the baseline designs are obtained using the CFX tool. While creating the grid topology and analysis structure of the basic design analysis, the validation study is accepted as the reference.

Figure 35 and Figure 36 illustrate the fan static pressure and efficiency curves for the baseline designs, respectively. According to the data presented in Figure 36 the optimal efficiency of the design centrifugal impeller is very close to the optimal efficiency of the baseline centrifugal impeller. The fan static pressure and total to static isentropic efficiency values, at the design point, are provided in Table 14. The 1D optimization study reveals that the fan static pressure and total to static isentropic efficiency are increased by 5.2% and 2.9%, respectively,

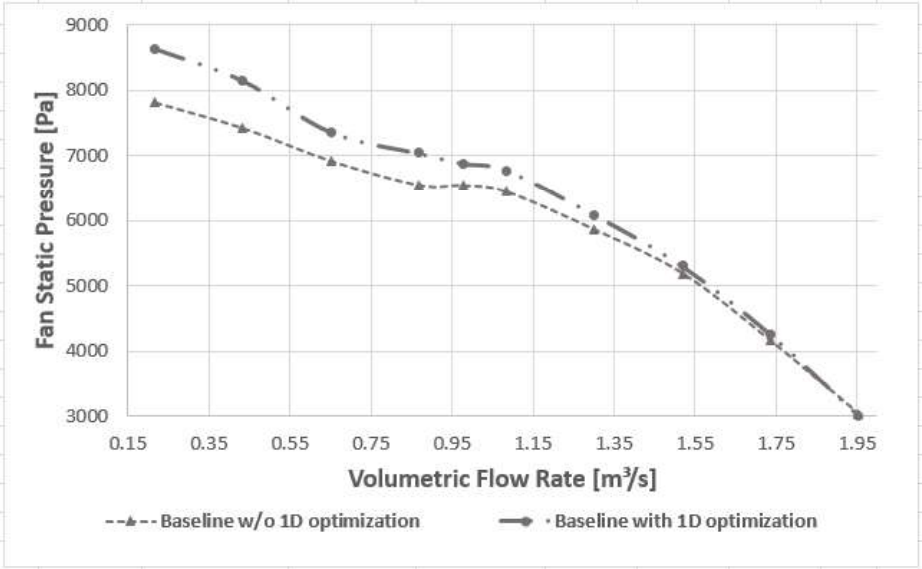

Figure 35. Baseline design fan static pressure curve

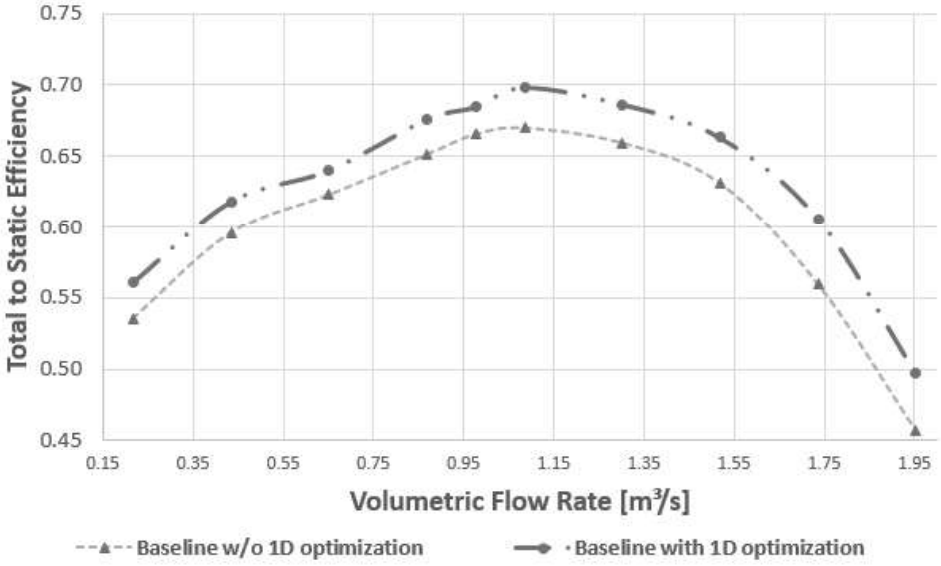

Figure 36. Baseline designs fan total to static efficiency curve

Table 14. Baseline designs fan static pressure and total to static efficiency values

Baseline Design	Fan Static Pressure	Efficiency
w/o 1D Optimization	6542.12	0.666
with 1D Optimization	6879.99	0.685
Percentage Increase	5.2	2.9

4.4 Optimization Procedure

In this study, an optimization study is performed by using ANSYS DesignXplorer with the Multi-Objective Genetic Algorithm (MOGA) together and he Kriging Response Surface Method (RSM). Design of Experiment (DoE) is an efficient method for gathering the data required to build the RSM. The RSM ability to predict outcomes is affected by how DoE distributes points within the design space [9]. According to Wang [22], the sampling method to be used in the experimental design should be suitable for the function to be estimated and should produce a minimum number of samples to accurately reflect the function of the meta-model. In the study by Khalfallah and Ghenait [25], it is stated that the sampling should be space-filling computer experiments. The Latin Hypercube Design (LHD) sampling method,

which is a gap-filling method, covers the design space, and provides a good spread. However, the Optimal Space Filling Design provides a more efficient spread along the design space. For these reasons, Optimal Space Filling Design with a max-min design type is used in the experimental design studies. In the experimental design, the design space is chosen ±10% of each input variable. Selected parameters and their range can be seen in Table 15.

Table 15. Input parameters design space

Parameters	Lower Bound	Baseline	Upper Bound
Axial Length (mm)	86.99	96.65	106.32
Tip Width (mm)	42.76	47.51	52.26
Inlet Height (mm)	66.09	73.43	80.78
Tip Radius (mm)	124.27	138.08	151.88

The designer can control the LHD sample size in terms of time, budget, or other constraints. There is no complete theory that governs that specifies how many design points are required to make LHD response surface models [22]. The quality of the response surface, however, is proportional to the size of the sample. Therefore, the surface quality should be always checked after the DoE study. It is known that a fixed minimum sample size is required based on the number of variables. However, it is typically preferable to use a larger sampling size than the minimum required in order to increase accuracy and have the possibility of estimating how good the meta model is [26]. For the linear and quadratic polynomial response surface, the minimum number of data points will be calculated in Equation 4.1 and Equation 4.2, respectively. Additionally, another option is to use a Central Composite Design sample size, as calculated in Equation 4.3. The sample size rises exponentially as the number of design variables increases.

$$n_{min} = 1 + k \tag{4.1}$$

$$n_{min} = 1 + 2k + \frac{k(k-1)}{2} = \frac{(k+1)(k+2)}{2} \tag{4.2}$$

$$n = 2^k + 2k + 1 \tag{4.3}$$

For the 4 variables, the required sample size for linear, quadratic, and CCD is 5, 15, and 25, respectively. In this study, 25 data points are used to train the meta-model. Response surface quality will be checked to assess whether the provided number of data points is sufficient or not. When necessary, refinement points are added to the meta-model to increase its accuracy.

Because extra dynamic pressure at the impeller outlet in centrifugal fans is wasted unless it is partially converted into static pressure by a diffuser, fan static pressure and total to static isentropic efficiency are used for the evaluation of fan performance [39]. Two objective functions, fan static pressure and total to static isentropic efficiency, are selected for this study.

Non-Dominated Sorting Genetic Algorithm-II (NSGA-II) is a powerful method for finding Pareto Optimal solutions in multi-objective optimization. NSGA-II employs a fast non-dominated sorting procedure, an elitist persevering strategy, and a parameterless niching strategy [30].

CHAPTER 5

RESULTS AND DISCUSSION

In the literature, second-order polynomial and Kriging are two response surface model, which is mostly used. Since Kriging fits the response surface from all design points, it is expected that goodness of fit measurements will always be good [23], therefore interpolation was made with the Kriging model, using both global and local approaches in the design field. Moreover, Kriging works especially well with space-filling designs [26]. In this study, goodness of fit curve for both second order and Kriging response model is observed. As seen in Figure 37 and Figure 38, prediction from the Kriging response surface is well-fitted with an observation from design points. Therefore, Kriging response model is preferred instead of second-order response surface model.

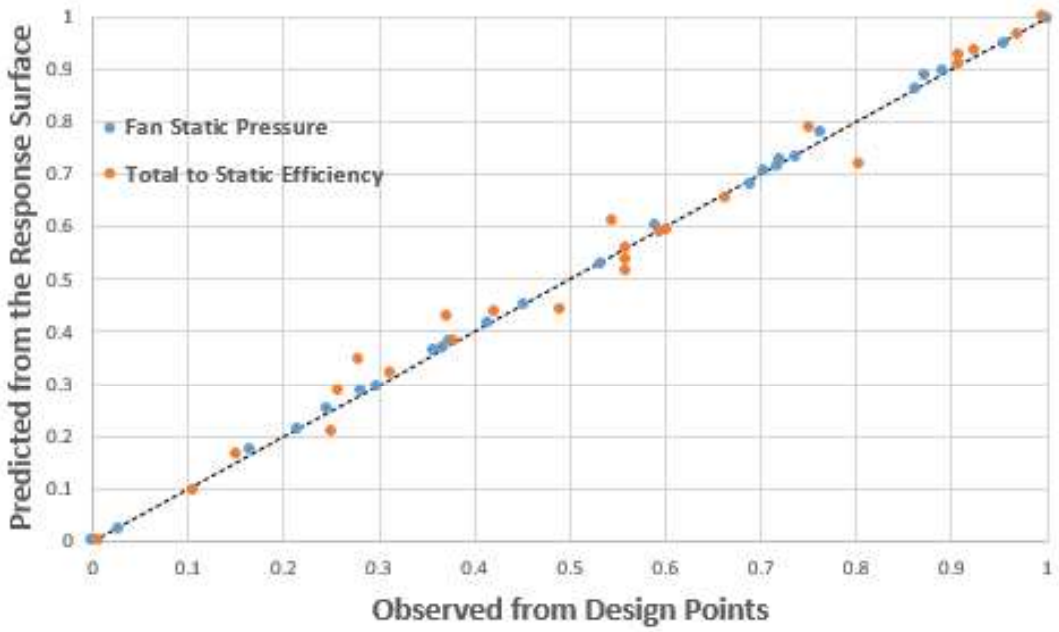

Figure 37. Goodness of fit curve for second-order polynomial RSM

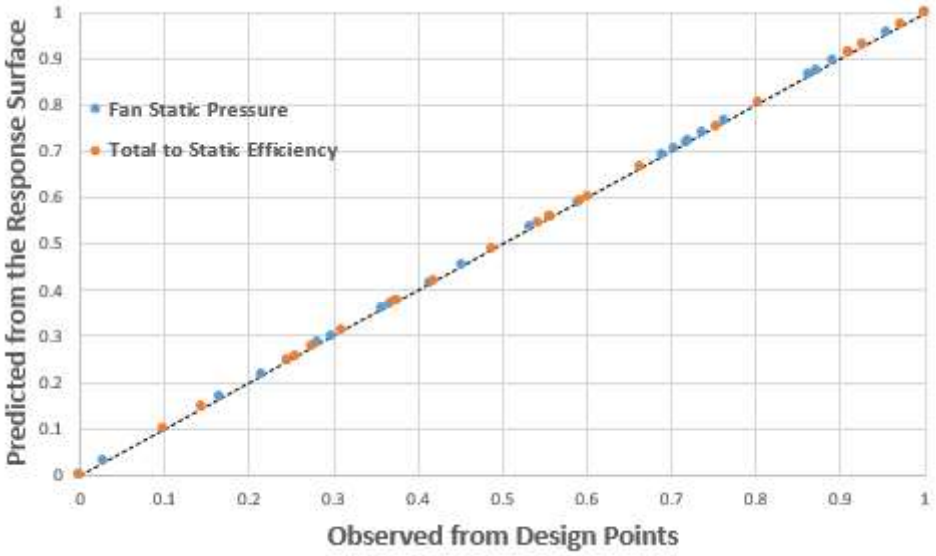

Figure 38. Goodness of fit curve for Kriging RSM

Sensitivity analysis is performed and parameters affecting the objective values mostly, are determined. Figure 39 indicates that tip radius has the greatest impact on fan pressure, whereas tip width has the least. The axial length and inlet height have nearly equal effects on fan pressure. However, while the fan pressure increases as the axial length increases, it decreases as the inlet height increases. As illustrated in Figure 40, the tip radius and inlet height have the greatest influence on the total to static isentropic efficiency. Total to static efficiency decreases with increasing tip radius and inlet height. Tip width and axial length show the same trend.

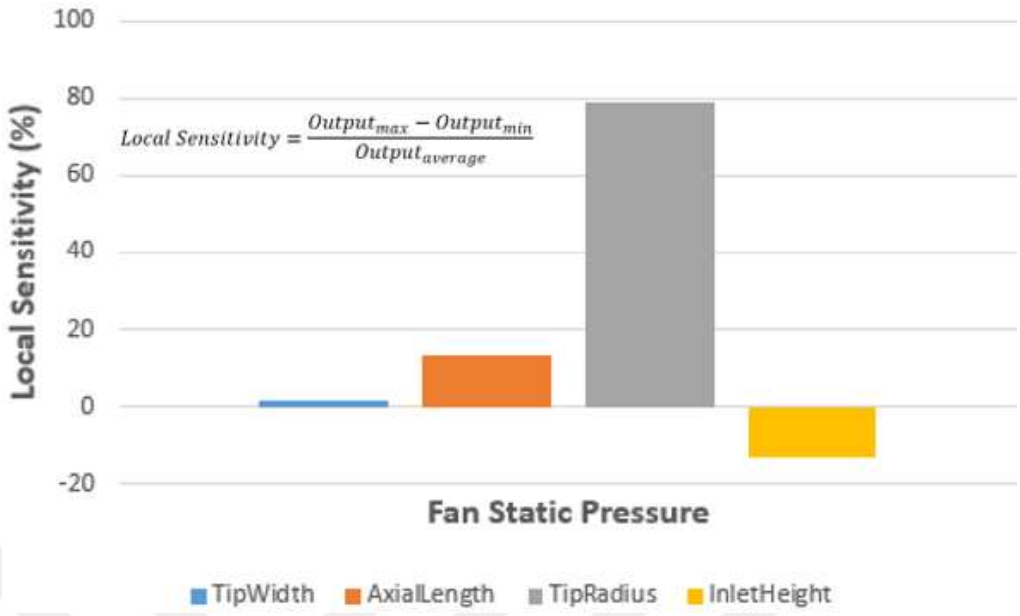

Figure 39. Fan Static Pressure sensitivity with respect to design variables

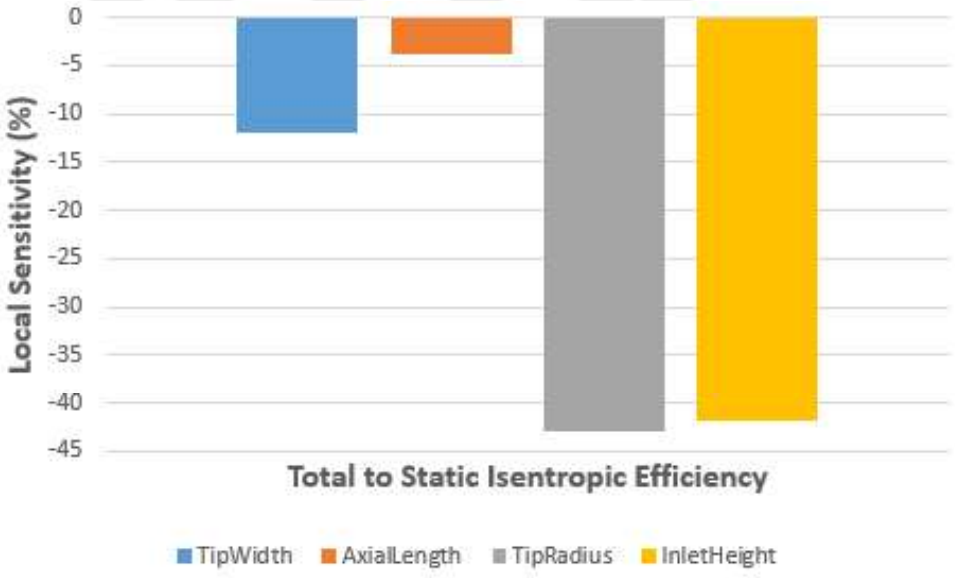

Figure 40. Total to static isentropic efficiency sensitivity regarding design variables

As seen in Figure 41, as the tip radius increases fan static pressure is increasing, however, it is decreasing as inlet height is increasing. Figure 42 shows there is a tip radius and inlet height interval where total to static efficiency is increasing. For the tip radius, and inlet height, these intervals are 128-136 mm and 68-72 mm. Besides that, total to static efficiency is decreasing with respect to tip radius and inlet height.

As seen in Figure 41 and Figure 42, there is no local maxima or minima in the response surface, which is also observed in other turbomachinery studies [9], [51]–[53].

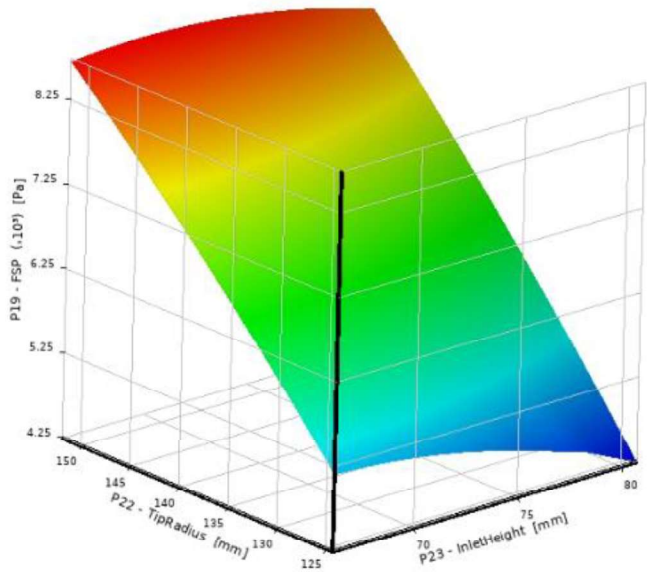

Figure 41. Fan Static Pressure Response Surface with respect to tip radius and inlet height

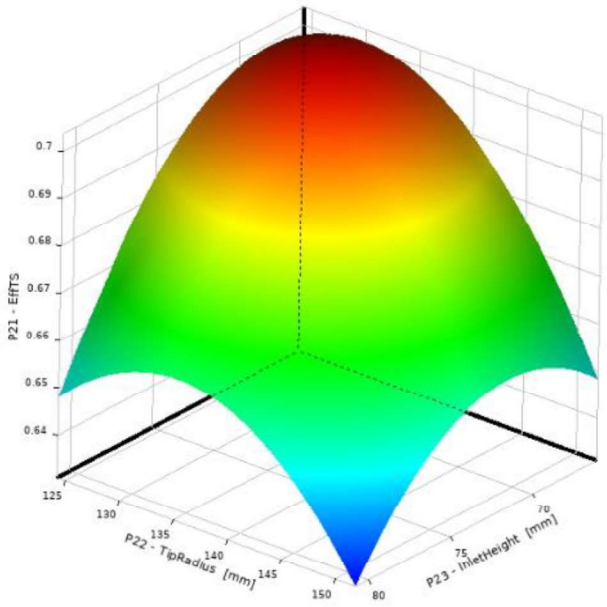

Figure 42. Total to Static Isentropic Efficiency Response Surface with respect to tip radius and inlet height

Figure 43 depicts the relationship between the parameters by using correlation plot generated by a trained Kriging Response Surface Model.

Parameters	Tip Width	Axial Length	Tip Radius	Inlet Height	Fan Static Pressure	Total-Static Efficiency
Tip Width	1	0.032842456	0.066185051	-0.020394554	0.070130592	-0.162545151
Axial Length	0.032842456	1	-0.036454571	-0.052514587	0.147763268	0.067963323
Tip Radius	0.066185051	-0.036454571	1	-0.020338983	0.960600167	-0.567713254
Inlet Height	-0.020394554	-0.052514587	-0.020338983	1	-0.198499583	-0.636899139
Fan Static Pressure	0.070130592	0.147763268	0.960600167	-0.198499583	1	-0.399055293
Total-Static Efficiency	-0.162545151	0.067963323	-0.567713254	-0.636899139	-0.399055293	1

Figure 43. Correlation plot by using the Kriging Response Surface Model

Figure 44 shows Pareto Optimal Solutions. Among the Pareto Optimal Solutions (POS), one candidate point is selected, which is indicated in Figure 44 by a red dot. In Table 16, the meta-model solution and CFD results are compared. It is found that fan static pressure and total to static isentropic efficiency, as compared to CFD results, are calculated with an error of 0.12% and 0.33%, respectively. For the selected size optimization impeller, 3D view can be seen in Figure 45.

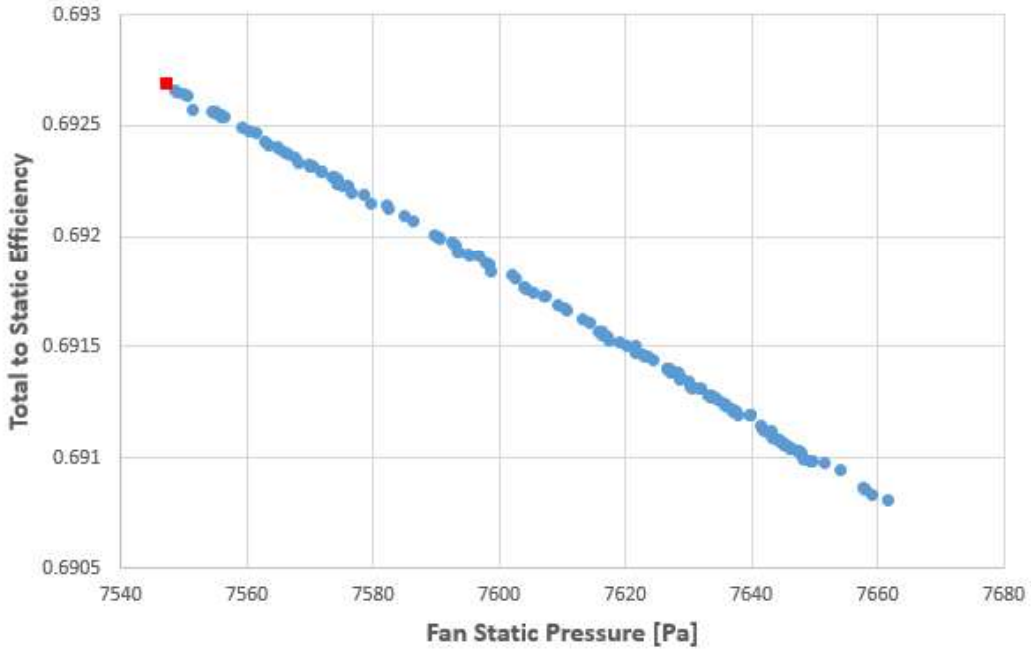

Figure 44. Pareto optimal solutions

Table 16. Meta-model and CFD results comparison

Objective Function	Meta-Model	CFD	Error %
Fan Static Pressure	7547 Pa	7538 Pa	0.12
Efficiency	0.693	0.69	0.33

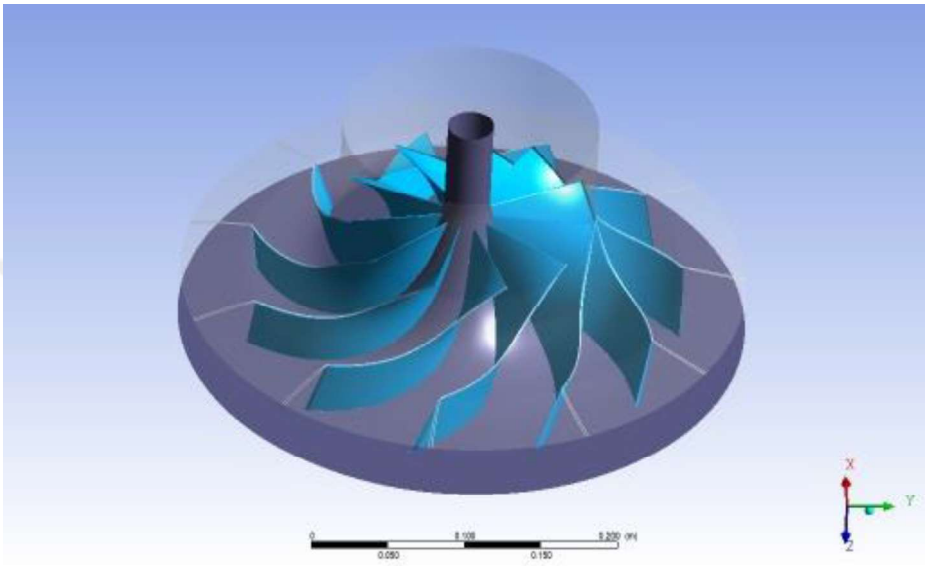

Figure 45. Size optimization impeller 3D view

Figure 46 and Figure 47 compare optimized centrifugal fan impeller fan static pressure and total to static isentropic efficiency to baseline. As can be seen, the fan static pressure rise is greater until 1.5 m^3/s, but then it decreases. Figure 47 illustrates that, at the design point, total to static isentropic efficiency is increased and remained nearly the same at off-design points, until 1.5 m^3/s, but then it starts to decrease suddenly. It can be deduced that the optimized impeller produces better total to static pressure rise with 1% increased efficiency at the design point, which is marked with a red dot, and nearly the same efficiency until 1.5 m^3/s.

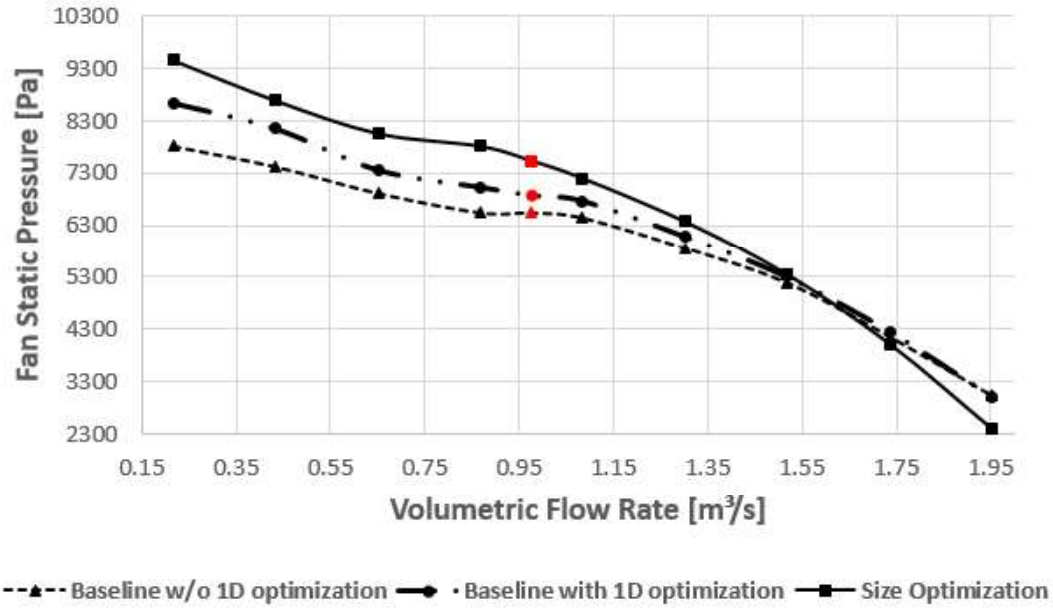

Figure 46. Fan Static Pressure comparison between baseline and optimized impeller. Red points correspond to the design point where the volumetric flow rate is 1 m3/s.

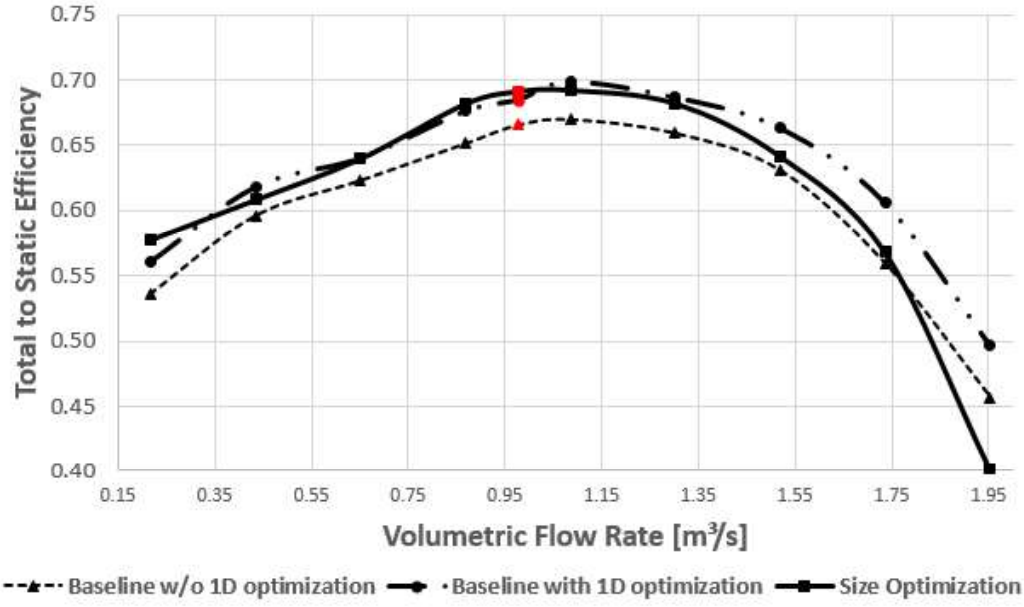

Figure 47. Total to Static efficiency comparison between baseline and optimized impeller. Red points correspond to the design point where the volumetric flow rate is 1 m3/s.

In order to see the flow distribution effect and associated losses, the baseline set and optimized impeller are compared using the entropy contours. Figure 48 Figure 49, and Figure 50, show entropy contours along the 20%, 50%, and 80% span,

respectively. Flow separation increases with increasing span percentage for the baseline and optimized impellers.

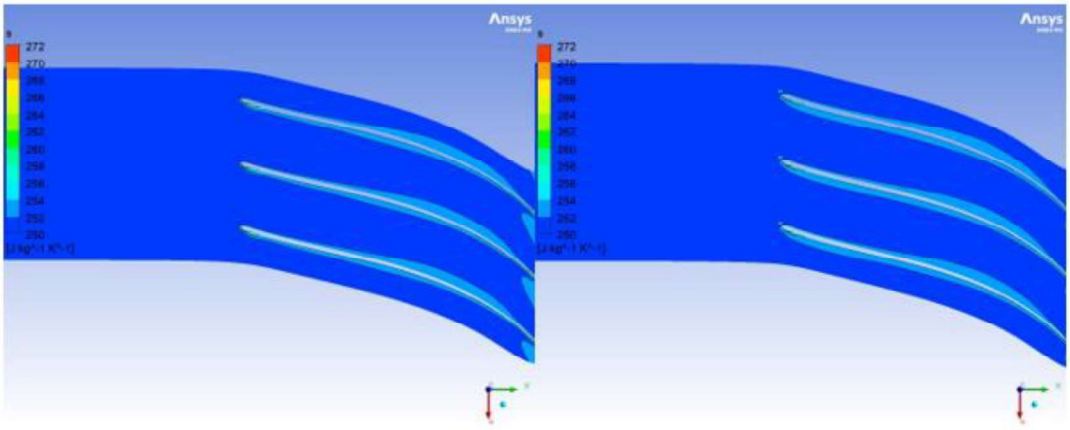

Figure 48. Entropy contours along 20% Span a) Baseline impeller b) Optimized impeller

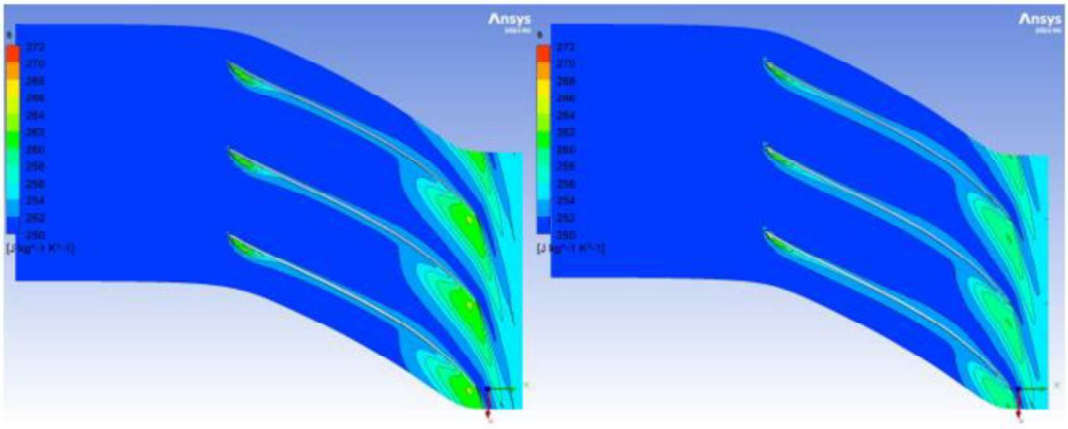

Figure 49. Entropy contours along 50% Span a) Baseline impeller b) Optimized impeller

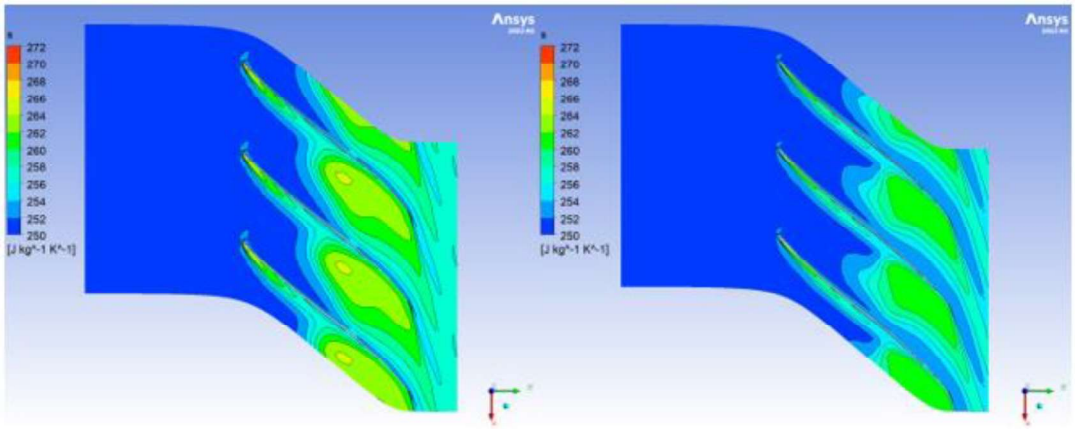

Figure 50. Entropy contours along 80% Span a) Baseline impeller b) Optimized impeller

In order to decrease separations for the baseline impeller, blade loading distribution is updated when the different relative velocity ratio of the 1D optimized impeller is established, while other parameters in Table 12 remain unchanged. Figure 51 depicts the effect of the varying relative velocity ratios considering the entropy contours and relative Mach number distribution at the 80% span. Flow separations and corresponding losses are observed to decrease as relative velocity increases. It is also seen in Figure 52, as the relative velocity ratio increases, flow separations reduce and air exits the impeller smoothly.

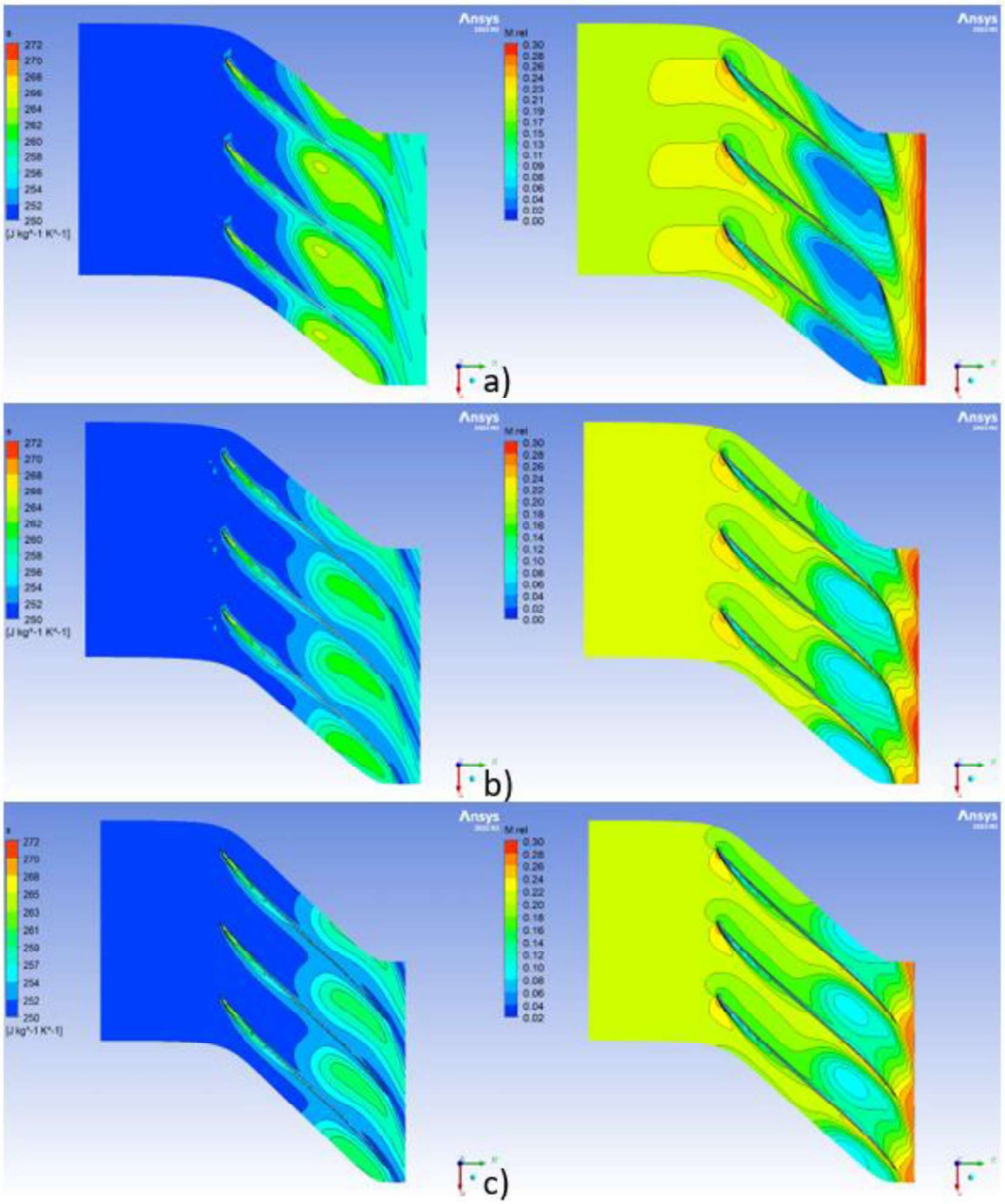

Figure 51. Entropy contours of 80% span at the left and relative Mach number distribution of 80% span at the right a) Relative velocity ratio=0.58, b) Relative velocity ratio=0.70, and c) Relative velocity ratio=0.85

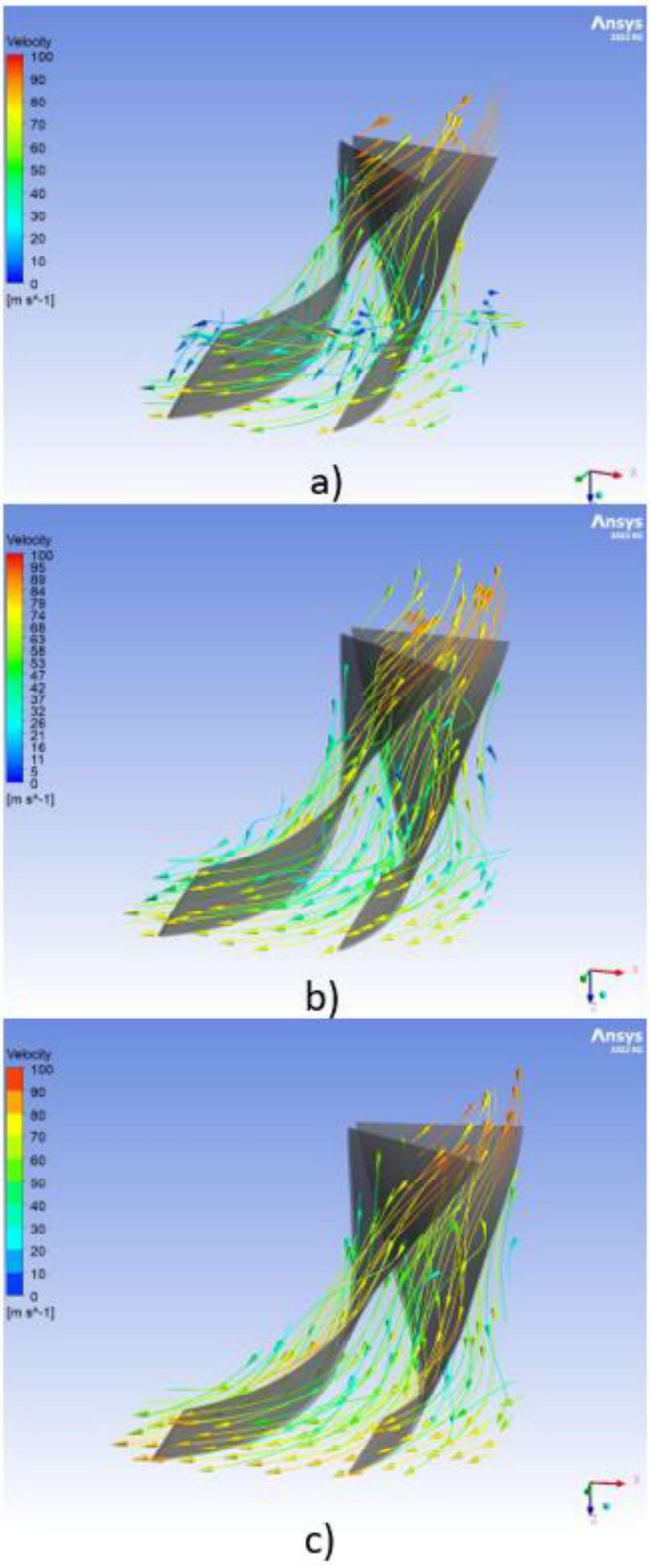

Figure 52. Velocity streamlines a) Relative velocity ratio=0.58, b) Relative velocity ratio=0.70, and c) Relative velocity ratio=0.85

As shown in Table 17, as the relative velocity ratio increases, the impeller diameter increases, and the tip width decreases. As a result of that total isentropic efficiency decreases correspondingly. It is also observed that the flow coefficient and head coefficient decrease with increasing relative velocity ratio.

Table 17. Effect of the relative velocity ratio on impeller parameters

Parameter	**0.58**	**0.7**	**0.85**
Impeller Diameter [mm]	276.15	289.39	307.02
Tip Width [mm]	47.507	35.548	26.443
Total Isentropic Efficiency	0.88	0.876	0.868
Flow Coefficient	0.098	0.086	0.072
Head Coefficient	0.624	0.571	0.513

CHAPTER 6

CONCLUSION AND FUTURE WORK

In this study, the impeller geometry of a backward-curved blade centrifugal fan was optimized by coupling the optimization algorithm with computational fluid dynamics simulations. The experimental results of the NASA LSCC verified the validity of the numerical model. The CFD simulations performed in ANSYS CFX flow solver with the $k-\omega$ SST turbulence model gave the best agreement with the experimental data; therefore, ANSYS CFX flow solver with the $k-\omega$ SST turbulence model was used in the optimization process.

In the optimization phase, the Kriging RSM was utilized and trained using 25 different designs. NSGA-II was used in the optimization study to determine the best solution among the POS. Fan static pressure and efficiency were increased by 8.34% and 0.96% at the design point, respectively. In conjunction with the optimal space-filling design, the Kriging method was shown to be effective for turbomachinery design optimization.

In order to improve the automated design procedure given in this thesis, the following topics can be considered in future studies:

- Our study focuses on the optimization of a centrifugal fan impeller only. In future studies, volute design and optimization can also be considered as a part of the optimization procedure.
- Extending the design space and increasing the number of design variables are two ways to enhance the 1D optimization presented in this thesis.
- An aerodynamic optimization approach is used in this investigation. Before constructing an impeller, structural optimization can be combined with aerodynamic optimization.

REFERENCES

[1] G. Gasparini, N. Motta, A. Gabrielli, and D. Colombo, “Gearbox loss of lubrication performance: Myth, art or science?,” in *40th European Rotorcraft Forum 2014*, 2014, vol. 2.

[2] K.-Y. Kim, A. Samad, and E. Benini, *Design Optimization of Fluid Machinery*. 2019.

[3] Z. C. Thaung, S. Zin Nyunt, and K. K. Swe, “Numerical Study on Flow Characteristics of Radial Tipped Impeller for Centrifugal Fan,” *IRE*, vol. 3, no. 2, 2019.

[4] T. Kebede, “Fluid Flow Analysis and Performance Prediction of a Radial Fan Using CFD,” Addis Ababa University, 2012.

[5] S. N. R. Neal Ellliott, “Fan and Pump Systems: Markets and Programs,” *Am. Counc. an Energy-Efficient Econ.*

[6] S. Wang, L. Zhang, Q. Zhang, and X. Ye, “Numerical investigation of entropy generation and optimization on a centrifugal fan,” *Adv. Sci. Lett.*, vol. 4, no. 6–7, 2011, doi: 10.1166/asl.2011.1634.

[7] B. Eck, *Fans; design and operation of centrifugal, axial-flow, and cross-flow fans*. Pergamon Press, 1973.

[8] A. H. Church, *Centrifugal Pump and Blowers*. John Wiley and sons, Inc., 1944.

[9] C. Zhu and G. Qin, “Design technology of centrifugal fan impeller based on response surface methodology,” in *American Society of Mechanical Engineers, Fluids Engineering Division (Publication) FEDSM*, 2010, vol. 1, no. PARTS A, B AND C, doi: 10.1115/FEDSM-ICNMM2010-30002.

[10] M. W. Heo, J. H. Kim, and K. Y. Kim, “Design optimization of a centrifugal

fan with splitter blades," *Int. J. Turbo Jet Engines*, vol. 32, no. 2, 2015, doi: 10.1515/tjj-2014-0026.

[11] J.-H. Kim, J.-H. Choi, and K.-Y. Kim, "Surrogate Modeling for Optimization of a Centrifugal Compressor Impeller," *Int. J. Fluid Mach. Syst.*, vol. 3, no. 1, 2010, doi: 10.5293/ijfms.2010.3.1.029.

[12] X. Shu, C. Gu, J. Xiao, and C. Gao, "Centrifugal compressor blade optimization based on uniform design and genetic algorithms," *Front. Energy Power Eng. China*, vol. 2, no. 4, 2008, doi: 10.1007/s11708-008-0083-5.

[13] S. Kim, J. Park, K. Ahn, and J. Baek, "Numerical investigation and validation of the optimization of a centrifugal compressor using a response surface method," *Proc. Inst. Mech. Eng. Part A J. Power Energy*, vol. 224, no. 2, 2010, doi: 10.1243/09576509JPE842.

[14] J. H. Kim, J. H. Choi, A. Husain, and K. Y. Kim, "Multi-objective optimization of a centrifugal compressor impeller through evolutionary algorithms," *Proc. Inst. Mech. Eng. Part A J. Power Energy*, vol. 224, no. 5, 2010, doi: 10.1243/09576509JPE884.

[15] J. H. Kim, J. H. Choi, A. Husain, and K. Y. Kim, "Design optimization of a centrifugal compressor impeller by multi-objective genetic algorithm," in *Proceedings of the ASME Fluids Engineering Division Summer Conference 2009, FEDSM2009*, 2009, vol. 2, doi: 10.1115/FEDSM2009-78486.

[16] J. H. Kim, J. H. Choi, and K. Y. Kim, "Design optimization of a centrifugal compressor impeller using radial basis neural network method," in *Proceedings of the ASME Turbo Expo*, 2009, vol. 7, no. PART A, doi: 10.1115/GT2009-59666.

[17] L. Zhang, S. Wang, C. Hu, and Q. Zhang, "Multi-objective optimization design and experimental investigation of centrifugal fan performance," *Chinese J. Mech. Eng. (English Ed.*, vol. 26, no. 6, 2013, doi:

10.3901/CJME.2013.06.1267.

[18] F. Meng, Q. Dong, Y. Wang, P. Wang, and C. Zhang, “Numerical optimization of impeller for backward-curved centrifugal fan by Response Surface Methodology (RSM),” *Res. J. Appl. Sci. Eng. Technol.*, vol. 6, no. 13, 2013, doi: 10.19026/rjaset.6.3719.

[19] Ç. Mert, “Design and optimization of a mixed flow compressor impeller using robust design methods,” Middle East Technical University, 2009.

[20] G. Avşar, A. A. Ezertaş, and Ö. Başkan Perçin, “Çok amaçlı optimizasyon metoduyla helikopter transmisyon yağ soğutma fan çarkının tasarımı,” 2022.

[21] S. S. Rao, *Engineering optimization: Theory and practice*. 2019.

[22] Z. Li and X. Zheng, “Review of design optimization methods for turbomachinery aerodynamics,” *Progress in Aerospace Sciences*, vol. 93. 2017, doi: 10.1016/j.paerosci.2017.05.003.

[23] ANSYS Inc., “Introduction to ANSYS DesignXplorer.” 2019.

[24] Siemens, “Heeds MDO,” 2021.

[25] S. Khalfallah, A. Ghenaiet, E. Benini, and G. Bedon, “Surrogate-based shape optimization of stall margin and efficiency of a centrifugal compressor,” *J. Propuls. Power*, vol. 31, no. 6, 2015, doi: 10.2514/1.B35543.

[26] A. Ryberg, R. D. Bäckryd, and N. Larsgunnar, “Metamodel-Based Multidisciplinary Design Optimization for Automotive Applications,” 2012.

[27] M. R. G. Meireles, P. E. M. Almeida, and M. G. Simões, “A comprehensive review for industrial applicability of artificial neural networks,” *IEEE Transactions on Industrial Electronics*, vol. 50, no. 3. 2003, doi: 10.1109/TIE.2003.812470.

[28] K. SUGIMURA, S. JEONG, S. OBAYASHI, and T. KIMURA, “Kriging-

Model-Based Multi-Objective Robust Optimization and Trade-Off Rule Mining of a Centrifugal Fan with Dimensional Uncertainty," *J. Comput. Sci. Technol.*, vol. 3, no. 1, 2009, doi: 10.1299/jcst.3.196.

[29] J. S. D. Seyedali Mirjalili, *Multi-Objective Optimization using Artificial Intelligence Techniques*. Springer, 2020.

[30] K. Deb, A. Pratap, S. Agarwal, and T. Meyarivan, "A fast and elitist multiobjective genetic algorithm: NSGA-II," *IEEE Trans. Evol. Comput.*, vol. 6, no. 2, 2002, doi: 10.1109/4235.996017.

[31] A. Kocatürk and B. Altunkaynak, "Çok Amaçlı Optimizasyon Problemlerinin NSGA-II Yaklaşımıyla Çözümü," 2019.

[32] M. D. Hathaway, R. M. Chriss, A. J. Strazisar, and J. R. Wood, "Laser Anemometer Measurements of the Three-Dimensional Rotor Flow Field in the NASA Low-Speed Centrifugal Compressor," 1995.

[33] M. D. Hathaway, J. R. Wood, and C. A. Wasserbauer, "NASA low-speed centrifugal compressor for 3-D viscous code assessment and fundamental flow physics research," in *Proceedings of the ASME Turbo Expo*, 1991, vol. 1, doi: 10.1115/91-GT-140.

[34] J. D. Denton, "Some limitations of turbomachinery CFD," in *Proceedings of the ASME Turbo Expo*, 2010, vol. 7, no. PARTS A, B, AND C, doi: 10.1115/GT2010-22540.

[35] O. F. Atac, J. E. Yun, and T. Noh, "Aerodynamic design optimization of a micro radial compressor of a turbocharger," *Energies*, vol. 11, no. 7, 2018, doi: 10.3390/en11071827.

[36] P. G. Tucker, "Trends in turbomachinery turbulence treatments," *Progress in Aerospace Sciences*, vol. 63. 2013, doi: 10.1016/j.paerosci.2013.06.001.

[37] R. M. Chriss, M. D. Hathaway, and J. R. Wood, "Experimental and computational results from the nasa lewis low-speed centrifugal impeller at

design and part-flow conditions," *J. Turbomach.*, vol. 118, no. 1, 1996, doi: 10.1115/1.2836607.

[38] L. Bourabia, S. Khalfallah, M. Cerdoun, and T. Chettibi, "An efficient methodology to generate optimal inputs for the preliminary design of centrifugal compressor impellers," *Proc. Inst. Mech. Eng. Part E J. Process Mech. Eng.*, vol. 234, no. 4, 2020, doi: 10.1177/0954408920927658.

[39] P. Epple, F. Durst, and A. Delgado, "A theoretical derivation of the Cordier diagram for turbomachines," *Proc. Inst. Mech. Eng. Part C J. Mech. Eng. Sci.*, vol. 225, no. 2, 2011, doi: 10.1243/09544062JMES2285.

[40] C. Xu, "Design experience and considerations for centrifugal compressor development," *Proc. Inst. Mech. Eng. Part G J. Aerosp. Eng.*, vol. 221, no. 2, 2007, doi: 10.1243/09544100JAERO103.

[41] M. Casey and C. Robinson, *Radial Flow Turbocompressors*. 2021.

[42] S. Lieblein, F. Schwenk, and R. Broderick, "Diffusion Factor For Estimating Losses And Limiting Blade Loadings In Axial-Flow-Compressor Blade Elements," 1953.

[43] E. Dick, *Fundamentals of Turbomachines*, vol. 109, no. 1. 2015.

[44] B. Lakshminarayana, "Fluid dynamics and heat transfer of turbomachinery," *Choice Rev. Online*, vol. 33, no. 10, 1996, doi: 10.5860/choice.33-5735.

[45] P. D. S.M. Yahya, "Turbines, Compressors and Fans, Fourth Edition," *Tata McGraw-Hill Publ. Co. Ltd.*, p. 923, 2011, [Online]. Available: https://www.accessengineeringlibrary.com/content/book/9780070707023.

[46] R. A. Van den Braembussche, "Numerical Optimization for Advanced Turbomachinery Design," in *Optimization and Computational Fluid Dynamics*, 2008.

[47] S. Pakle and K. Jiang, "Design of a transonic centrifugal compressor for

High-speed turbomachinery," *Proc. Inst. Mech. Eng. Part C J. Mech. Eng. Sci.*, vol. 235, no. 11, 2021, doi: 10.1177/0954406220953171.

[48] R. A. Van Den Braembussche *et al.*, "Multidisciplinary multipoint optimization of a transonic turbocharger compressor," in *Proceedings of the ASME Turbo Expo*, 2012, vol. 8, no. PARTS A, B, AND C, doi: 10.1115/GT2012-69645.

[49] K. Bamberger and T. Carolus, "A novel optimization based design method for centrifugal fans," 2017, doi: 10.29008/etc2017-326.

[50] S. Pakle and K. Jiang, "Design of a high-performance centrifugal compressor with new surge margin improvement technique for high speed turbomachinery," *Propuls. Power Res.*, vol. 7, no. 1, 2018, doi: 10.1016/j.jppr.2018.02.004.

[51] K. Alawadhi, B. Alzuwayer, T. A. Mohammad, and M. H. Buhemdi, "Design and optimization of a centrifugal pump for slurry transport using the response surface method," *Machines*, vol. 9, no. 3, 2021, doi: 10.3390/machines9030060.

[52] F. Meng, Q. Dong, P. Wang, and Y. Wang, "Multiobjective optimization for the impeller of centrifugal fan based on response surface methodology with grey relational analysis method," *Adv. Mech. Eng.*, vol. 2014, 2014, doi: 10.1155/2014/614581.

[53] G. Peng, S. Hong, H. Chang, Z. Zhang, and F. Fan, "OPTIMIZATION DESIGN OF MULTISTAGE PUMP IMPELLER BASED ON RESPONSE SURFACE METHODOLOGY," *J. Theor. Appl. Mech.*, vol. 59, no. 4, 2021, doi: 10.15632/jtam-pl/141939.